INL/MIS-16-38127-D
DE-EE0007159
Rev. 1

The Snake River Geothermal Consortium is a research partnership focused on advancing geothermal energy, hosted by Idaho National Laboratory.

Updated Site Characterization Data Inventory

May 2016

SRG Consortium | Snake River Geothermal

FORGE U.S. Department of Energy

INL/MIS-16-38127-D
Rev. 1

Updated Site Characterization Data Inventory

May 2016

Snake River Geothermal Consortium
Hosted by Idaho National Laboratory
Idaho Falls, Idaho

www.snakerivergeothermal.org

Prepared for the
U.S. Department of Energy
Office of Energy Efficiency and Renewable Energy
Under DOE Idaho Operations Office
Contract DE-AC07-05ID14517

CONTENTS

FIGURES

TABLES

ACRONYMS

EGS	enhanced geothermal systems
ESRP	Eastern Snake River Plain
FORGE	Frontier Observatory for Research in Geothermal Energy
GPS	Global Positioning System
GRRA	Geothermal Resource Research Area
INL	Idaho National Laboratory
MT	magnetotellurics
PSHA	probabilistic seismic hazard analysis
SMU	Southern Methodist University
SRP	Snake River Plain
TDS	total dissolved solid
USGS	United States Geological Survey

Updated Site Characterization Data Inventory

(Sections containing site characterization data that have been updated since the Phase 1 version of this document are indicated by an asterisk.)*

1. DATA MADE AVAILABLE THROUGH THE GEOTHERMAL DATA REPOSITORY ARCHIVE

Data collected and data products developed during Phase 1 of the Frontier Observatory for Research in Geothermal Energy (FORGE) project have been uploaded to the Geothermal Data Repository (GDR) to provide public access to relevant information for the proposed FORGE site on the Snake River Plain (SRP) in Idaho. This FORGE site will be located at the Idaho National Laboratory (INL) Site and operated by the Snake River Geothermal Consortium (SRGC).

The data uploaded to the GDR include sources used for characterization of the FORGE site and for development of the FORGE conceptual geologic model. These data provide information about seismic events, groundwater, geomechanical models, gravity surveys, magnetics, resistivity, magnetotellurics (MT), rock physics, stress, and geology. The site characterization data can be accessed, when released for public access, at https://gdr.openei.org/submissions/793. Data submitted to the GDR includes the following types:

1.1 Well Data Submissions

Pertinent data from deep wells on the INL Site, including Boreholes INEL-1, WO-2, and USGS-142, are included as links to separate data collections, as follows:

- For INEL-1, https://gdr.openei.org/submissions/792
- For WO-2, https://gdr.openei.org/submissions/791
- For USGS-142, https://gdr.openei.org/submissions/790.

1.2 JewelSuite Model

- Model1.wrl
- Model2.wrl

1.3 Petrel Model

- No outflow model
- Outflow model

1.4 Papers

1.4.1 Geologic Setting

Anders, M.H., Rodgers, D.W., Hemming, S.R., Saltzman, J., DiVenere, V.J., Hagstrum, J.T., Embree, G.F., and Walter, R.C., 2014, A fixed sublithospheric source for the late Neogene track of the Yellowstone hotspot: Implications of the Heise and Picabo volcanic fields: Journal of Geophysical Research, v. 119, p. 2871–2906, doi:10.1002/2013JB010483.

DeNosaquo, K., Smith, R., and Lowry, A., 2009, Density and lithospheric strength models of the Yellowstone–Snake River Plain volcanic system from gravity and heat flow data: Journal of Volcanology and Geothermal Research, v. 188, no. 1–3, p. 108–127, doi:10.1016/j.jvolgeores.2009.08.006.

Leeman, W., Annen, C., and Duffek, J., 2008, Dynamics of Crustal Magma Transfer, Storage and Differentiation, eds., Annen, C., and Zellmer, G., Geological Society, London, Special Publications 304, p. 235–259, DOI: 10.1144/SP304.12.

Leeman, W., Schutt, D., and Hughes, S., 2009, Thermal structure beneath the Snake River Plain: Implications for the Yellowstone hotspot: Journal of Volcanology and Geothermal Research, v. 188, no. 1–3, p. 57–67, doi:10.1016/j.jvolgeores.2009.01.034.

McCurry, M., McLing, T., Smith, R., Hackett, W., Goldsby, R., Lochridge, W., Podgorney, R., Wood, T., Pearson, D., Welhan, J., and Plummer, M., 2016, Geologic Setting of the Idaho National Laboratory Geothermal Resource Research Area, *in* Proceedings, 41st Workshop on Geothermal Reservoir Engineering, Stanford University, Stanford, California, SGP-TR-209.

McLing, T. L., Smith R. P., Blackwell D.D., Roback, R. C., and Sondrup A. J. Wellbore and Groundwater Temperature Distribution Eastern Snake River Plain, Idaho; Implications for Groundwater Flow and Geothermal Potential, Journal of Volcanology and Geothermal Research 320 (2016) 144–155

McQuarrie, N., and Rodgers, D., 1998, Subsidence of a volcanic basin by flexure and lower crustal flow: The eastern Snake River Plain, Idaho: Tectonics, v. 17, no. 2, p. 203–220.

Podgorney, R., McCurry, M., Wood, T., McLing, T., Ghassemi, A., Welhan, J., Mines, G., Plummer, M., Moore, J., Fairley, J., and Wood R., 2013, Enhanced Geothermal System Potential for Sites on the Eastern Snake River Plain, Idaho: GRC Transactions, v. 37.

1.4.2 Geomechanical Model

Bakshi, R., Halvaei, M., and Ghassemi, A., 2016, Geomechanical characterization of core from the proposed FORGE laboratory on the eastern Snake River Plain, Idaho: *in* Proceedings, 41st Workshop on Geothermal Reservoir Engineering, Stanford University, Stanford, California, SGP-TR-209.

1.4.3 Groundwater Data

Dobson, P., Kennedy, B., Conrad, M., McLing, T., Mattson, E., Wood, T., Cannon, C., Spackman, R., van Soest, M., and Robertson, M., 2015, He isotopic evidence for undiscovered geothermal systems in the Snake River Plain: *in* Proceedings, 40th Workshop on Geothermal Reservoir Engineering, Stanford University, Stanford, California, SGP-TR-204.

McLing, T., Smith, R., and Johnson, T., 2002, Chemical characteristics of thermal water beneath the eastern Snake River Plain: Geological Society of America Special Paper 353.

Travis, L., Smith, R.P., Smith, R.W., Blackwell, D.D., Roback, R.C., and Sondrup, A.J., 2016, Wellbore and groundwater temperature distribution eastern Snake River Plain, Idaho: Implications for groundwater flow and geothermal potential: Journal of Volcanology and Geothermal Research, doi: 10.1016/j.jvolgeores.2016.04.006.

Plummer, M., Palmer, C., McLing, T., and Sondrup, A., 2016, Modeling Heat Flow in the Eastern Snake River Plain Aquifer, *in* Proceedings, 41st Workshop on Geothermal Reservoir Engineering, Stanford University, Stanford, California, SGP-TR-209.

Welhan, J., 2015, Thermal and Trace-Element Anomalies in the Eastern Snake River Plain Aquifer: Toward a conceptual model of the EGS resource: GRC Transactions, v. 39, p. 363–375.

Welhan, J., 2016, Thermal and Geochemical Anomalies in the Eastern Snake River Plain Aquifer: Contributions to a Conceptual Model of the Proposed FORGE Test Site: *in* Proceedings, 41st Workshop on Geothermal Reservoir Engineering, Stanford University, Stanford, California, SGP-TR-209.

1.4.4 Regional Geophysical Characterization

1.4.4.1 Gravity

Mabey, D., 1978, Regional gravity and magnetic anomalies in the eastern Snake River Plain, Idaho: Journal of Research of the U.S. Geological Survey, v. 6, no. 5, p. 553–562.

1.4.4.2 Magnetic

1.4.4.3 MT Data

Kelbert, A. and Egbert, G., 2012, Crust and upper mantle electrical conductivity beneath the Yellowstone Hotspot Track: Geology, v. 40 no. 5, p. 447–450.

Stanley, W.D., 1982, Magnetotelluric soundings on the Idaho National Engineering Laboratory facility, Idaho: Journal of Geophysical Research: Solid Earth, v. 87, no. B4, p. 2683–2691.

Stanley, W.D., Boehl, J., Bostick, F. and Smith, H., 1977, Geothermal significance of magnetotelluric soundings in the eastern Snake River Plain – Yellowstone Region: Journal of Geophysical Research, v. 82, no. 17.

Wannamaker, P., and Maris, V., 2016, Re-Inversion of Long-Period MT Data over the Eastern Snake River Plain, Idaho: In support of Phase I of the Idaho National Laboratory FORGE Project.

1.4.4.4 Resistivity

Zohdy, A.A.R, and Stanley, W.D., 1973, Preliminary interpretation of electrical sounding curves obtained across the Snake River Plain from Blackfoot to Arco, Idaho: U.S. Geological Survey Open-File Report 73-0370.

1.4.4.5 Seismic

Pankratz, L., and Ackerman, H., 1982, Structure Along the Northwest Edge of the Snake River Plain Interpreted from Seismic Refraction: Journal of Geophysical Research, v. 87, no. B4, p. 2676–2682.

Peng, X., and Humphreys, E., 1998, Crustal velocity structure across the eastern Snake River Plain and the Yellowstone swell: Journal of Geophysical Research, 103 (B4), p. 7171–7186.

Smith, R.B. Schilly, M., Braile, L., Ansorge, J., Lehman, J., Baker, M., Prodehl, C., Healy, J., Mueller, S., and Greensfelder, R., 1982, The 1978 Yellowstone – Eastern Snake River Plain Seismic Profiling Experiment: Crustal structure of the Yellowstone Region and experiment design: Journal of Geophysical Research, v. 87 no. B4, p. 2583–2596.

Sparlin, M., and Braile, L., 1982, Crustal structure of the Eastern Snake River Plain determined from ray trace modeling of seismic refraction data: Journal of Geophysical Research, v. 87, no. B4, p. 2619–2633.

1.4.5 Rock Physics

Grana, D., Verma, S., and Podgorney, R., 2016, Rock Physics Modeling for the Potential FORGE Site on the Eastern Snake River Plain, Idaho, *in* Proceedings, 41st Workshop on Geothermal Reservoir Engineering, Stanford University, Stanford, California, SGP-TR-209.

1.4.6 Seismic Stations

Carpenter, N., Payne, S., Hodges, J., and Berg, R., 2011, INL Seismic Monitoring Annual Report January 1, 2010 – December 31, INL/EXT-11-23143.

Payne, S., Hodges, J., Berg, R., and Bruhn, D., 2012, INL Seismic Monitoring Annual Report January 1, 2011 – December 31, 2011, INL/EXT-12-27770.

Payne, S., Bruhn, D., Hodges, J., and Berg, R., 2014, INL Seismic Monitoring Annual Report January 1, 2012 – December 31, 2012, INL/EXT-14-33937.

1.4.7 Stress

Furlong, K., 1979, An analytic stress model applied to the Snake River Plain (Northern Basin and Range Province, U.S.A.): Tectonophysics, v. 58, no. T11-T15.

Moos, D., and Barton, C., 1990, In-situ Stress and Natural Fracturing at the INEL Site, Idaho_EGG-NPR-10631.

Payne, S., McCaffrey, R., and King, R., 2008, Strain rates and contemporary deformation in the Snake River Plain and surrounding Basin and Range from GPS and seismicity: Geology, v. 36, no. 8, p. 647–650, doi: 10.1130/G25039A.1.

2. RESOURCE CHARACTERISTICS

The proposed FORGE site is a "greenfield" basement enhanced geothermal systems (EGS) resource.

3. THERMAL CHARACTERISTICS

3.1 Introduction

High temperatures exist at relatively shallow depths in the Eastern Snake River Plain (ESRP) as a result of its volcanic genesis. The subsurface of the ESRP consists of thick rhyolitic ash-flow tuffs overlain by >1 km (>0.6 mi) of Quaternary period basaltic flows. The rhyolitic volcanic rocks at depth are the product of super-volcanic eruptions associated with the Yellowstone Hotspot. These rocks become progressively younger to the northeast, toward the Yellowstone Plateau (Hughes et al., 1999; Pierce and Morgan, 1992). The younger basalt layers are the result of many low-volume, monogenetic, shield-forming eruptions of short duration that emanated from northwest-trending volcanic rifts in the wake of the Yellowstone Hotspot (Hughes et al., 1999). A thermal anomaly extends deep into the mantle beneath the ESRP, and the region has some of the highest calculated heat fluxes in North America.

The thick sequences of coalescing basalt flows with interlayered fluvial and eolian sediments in the ESRP constitute a very productive aquifer system above the rhyolitic ash-flow tuffs (Nielson and Shervais, 2014; Shervais et al., 2013; Whitehead, 1992). Horizontal water flow, which originates as snowmelt from the Yellowstone Plateau and surrounding mountain basins, transports heat laterally (McLing et al 2016; Morse and McCurry, 2002) within the ESRP aquifer and thereby suppresses the upward heat flux above the aquifer. A conceptual model of the aquifer system overlying the geothermal heat source is provided in Figure 1.

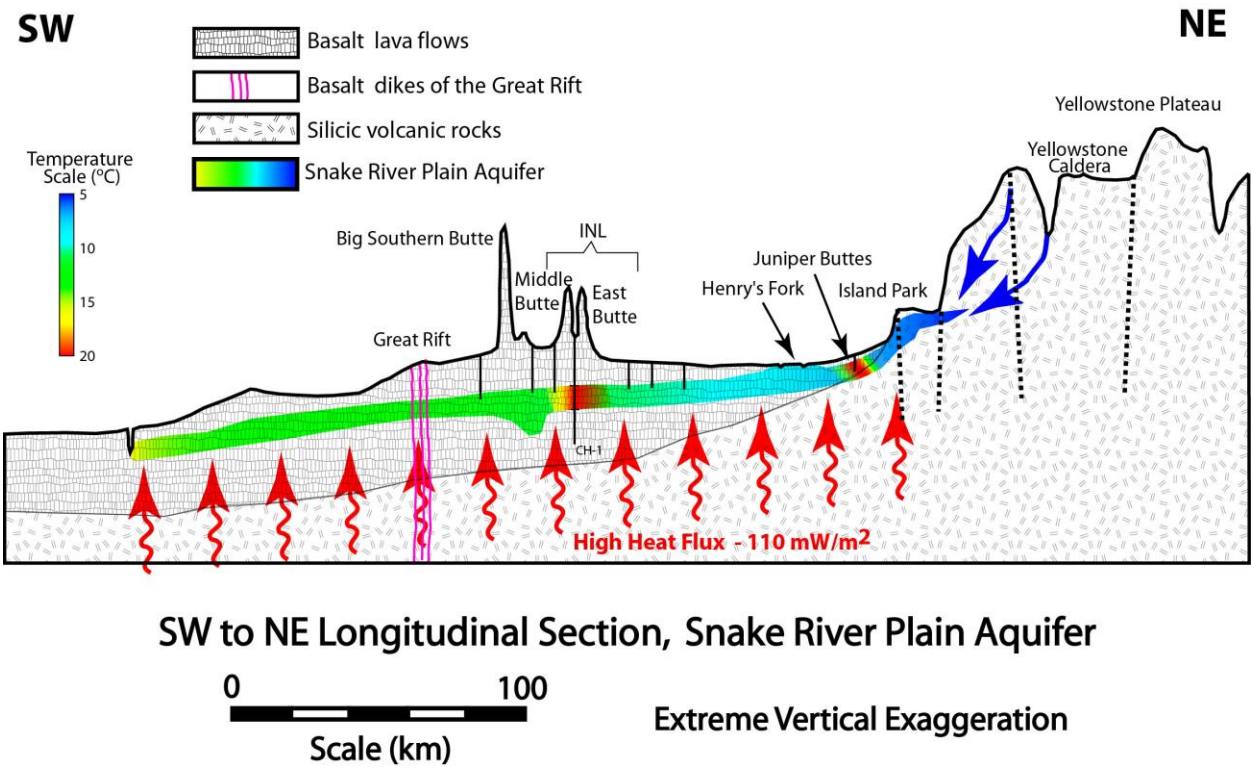

Figure 1. Conceptual model for heating of groundwater along the central axis of the SRP (McLing et al 2016).

Heat fluxes in the basalt flows are typically greatest on the margins of the SRP and lowest along the axis (center) of the plain, where vertical heat flux is suppressed by the ESRP aquifer. Beneath the aquifer, however, thermal gradients are also elevated well above typical gradients, likely reflecting heat flows associated with the intrusion of mafic magmas into mid-crustal sill complex (Shervais et al., 2011). High thermal fluxes in the ESRP were first documented in the early 1970s (Brott et al., 1976). Heat flow values of 110 mW/m^2 have been calculated below the ESRP aquifer, and values over 150 mW/m^2 have been projected for depths to 6 km (4 mi) (Blackwell and Richards, 2004). High heat fluxes across the ESRP, recent volcanic activity, and the occurrence of numerous peripheral hot springs demonstrate the presence of unexploited geothermal resources in the ESRP (McLing et al., 2016; Nielson and Shervais, 2014) with the potential for development of one or more conventional or enhanced geothermal reservoirs. In particular, the lower welded rhyolite ash-flow tuff zone may have exploitable heat sources that can be tapped by EGS development. The proposed study site (Figure 2) is located at the GRRA, which is on the western boundary of the INL Site near the southern toe of the Lost River Range. Abundant groundwater temperature data collected from ESRP (Figure 3) indicate that the study area is located atop an area of anomalously high groundwater temperatures that extends approximately 90 km (56 mi) to the southwest, through the Craters of the Moon volcanic area. High groundwater temperatures in that area likely reflect a combination of higher-than-average heat flux and minimal horizontal groundwater flow, where the aquifer is thin or nonexistent (McLing et al., 2016). This conclusion is supported by studies that have investigated the thickness of the upper active part of the ESRP aquifer (McLing et al., 2016; Morse and McCurry, 2002).

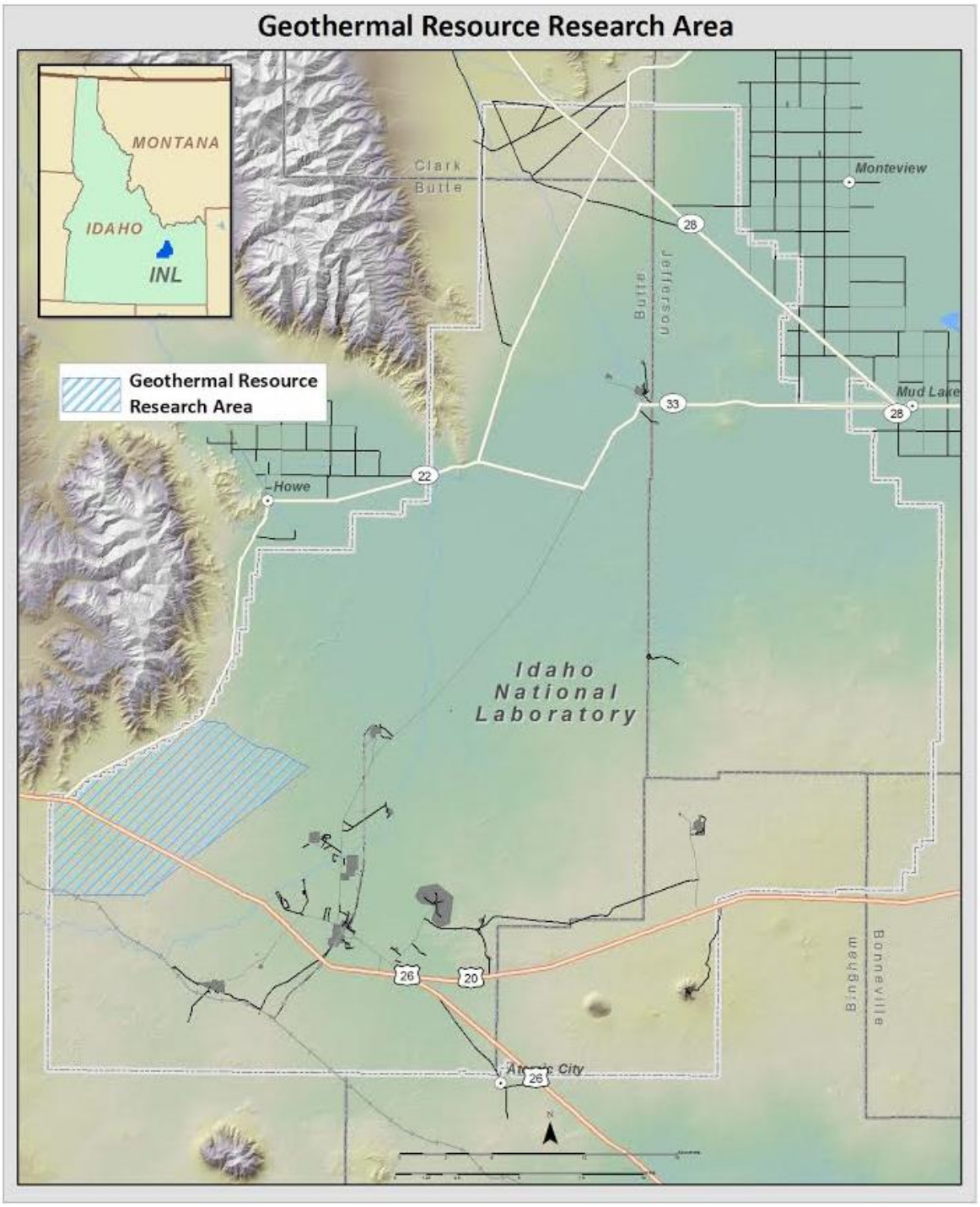

Figure 2. Location of the GRRA on the INL Site.

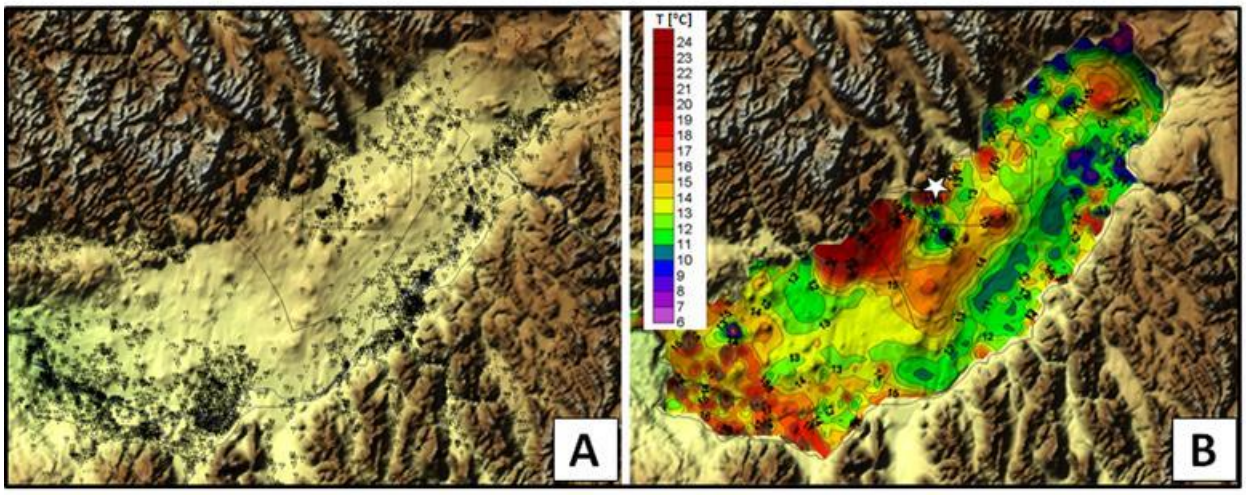

Figure 3. (A) Location of data points on the ESRP used to construct the (B) groundwater temperature map for the ESRP aquifer. Star shows location of the GRRA.

3.2 Bottomhole Temperature Measurements

Deep subsurface temperature measurements are available from bottomhole-temperature measurements obtained during drilling and from several continuous wire-line logs of wells and boreholes in the SRP. Most recently, the Hotspot Project (Nielson et al., 2012), which was designed to investigate the geothermal potential of the SRP through coring and scientific evaluation, obtained temperature logs from three deep core holes in the SRP. Temperature measurements from the Hotspot Project's hole south of the GRRA, at Kimama, Idaho, indicate that the SRP freshwater aquifer extends as deep as 965 m (0.6 mi) in that area and that the underlying temperature gradient is 74.5°C/km (4.1°F/100 ft). The corehole in the town of Kimberly, Idaho, reached a depth of 1,959 m (6,427 ft) and demonstrated a resource of >50°C (>122°F) from 800 m (2,625 ft) to the bottom of the hole. Prior to the Hotspot Project, the deepest measured bottomhole temperature from near GRRA was from INEL-1, a 3,160-m (10,365-ft)-deep geothermal test well drilled in 1978. Temperature at the bottom of the INEL-1 borehole was measured at 150°C (302°F) on May 24, 1979 (Doherty et al., 1979; Mann, 1986; Prestwich and Bowman, 1980).

Vertical temperature profiles and groundwater chemistry from deep boreholes at the INL Site indicate that the ESRP aquifer is composed of two systems: an upper system of fast-moving, cold water and a deep, geothermally heated confining zone. The shallow (or productive) portion of the aquifer extends from the water table (60 to 200 m [197 to 656 ft] below land surface) to a depth of 200 to 500 m (656 to 1,640 ft) below land surface. Temperatures in this portion of the aquifer, which is the primary water supply for the region, are approximately 9 to 15°C (48 to 59°F); seepage velocities are 1.5 to 10.5 m/day (4.9 to 34.4 ft/day), and chemistry is Ca-Mg-HCO3 dominated (Mann, 1986; Prestwich and Bowman, 1980; McLing et al., 2016). In the deeper geothermal confining zone, seepage velocities are 0.006 to 0.09 m/day (0.02 to 0.30 ft/day), and water chemistry is low in total dissolved solids (TDSs) and is classified as Na-K-HCO3 water type (Mann, 1986; McLing et al., 2002). The boundary between these two systems is generally well defined and marked by changes in geothermal gradient, chemistry, and the presence of diagenetic mineralization (Morse and McCurry, 2002). Temperature profiles from nine deep wells (Figure 4) demonstrate the dramatic break in slope that occurs at the boundary between the two systems, with a nearly isothermal vertical gradient in the upper aquifer to a linear gradient in the deeper system. Below the transition, there is also an increase in diagenetic minerals (Morse and McCurry, 2002) that indicates the vertical position of the transition has evolved over time. The alteration minerals demonstrate

sealing of pore space within the aquifer, which dramatically reduces permeability and flow, so that heat transfer is conductive rather than advection that dominates the temperature distribution in the lower portion of the aquifer.

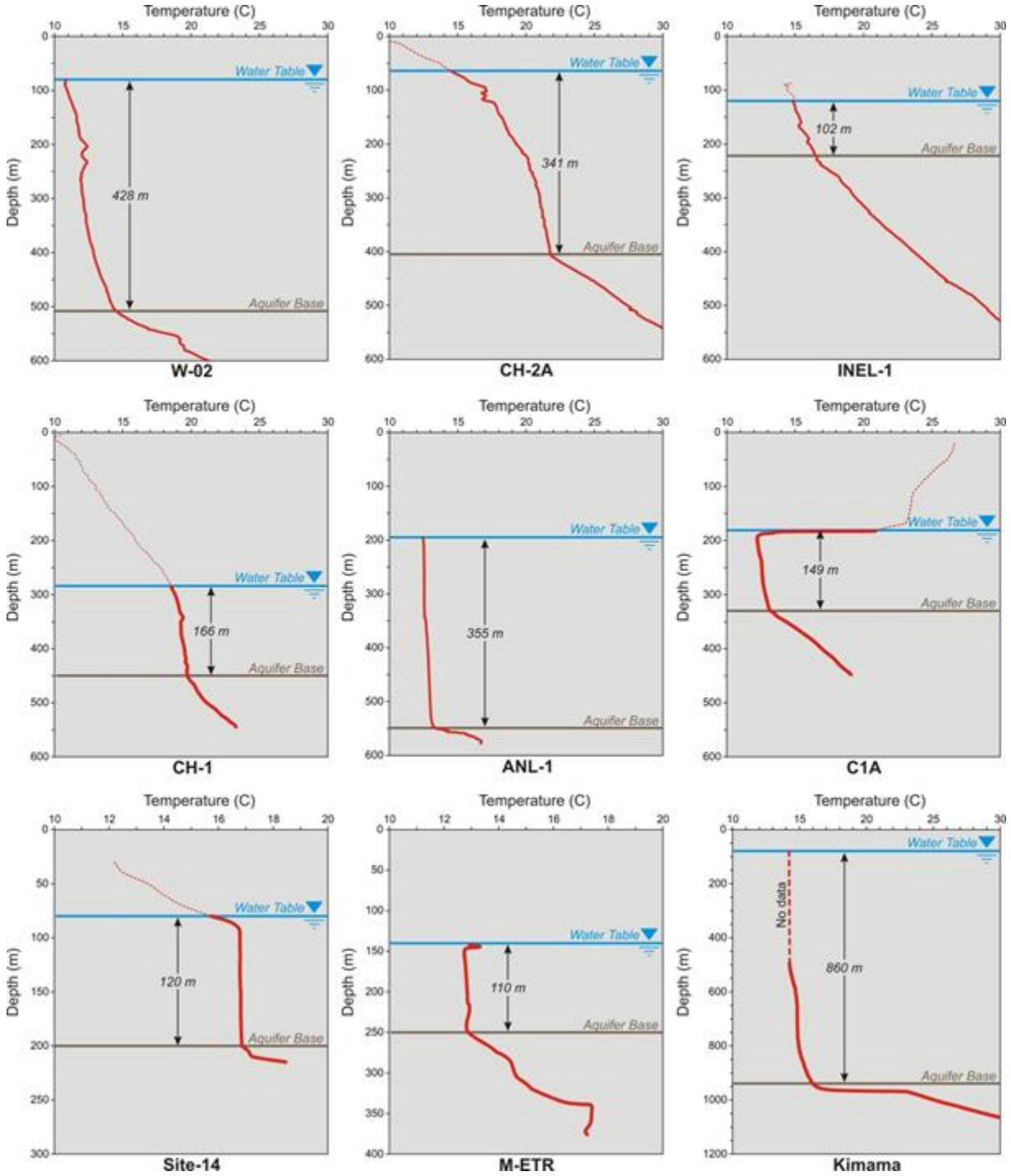

Figure 4. Downhole temperature logs of the deep wells on the INL site and Kimama Well drilled for the Hotspot Project. These temperature logs show the effective thickness of the aquifer but do not show, in all cases, the temperature profile for the total depth of the wells (McLing et al., 2016).

Similarly, abrupt changes across the cold-water aquifer to thermal water boundary are seen in other volcanic terrains such as the Cascade Range (Morse and McCurry, 2002), where deep systems with high-vertical heat flux are also masked by cold, shallow aquifers. Using chemical, thermal, and mineralogical breaks as a guide, the cold-water aquifer thickness in the GRRA (Figure 4) ranges from a few tens of meters on its western edge to a maximum of about 100 m (328 ft) on its eastern edge.

3.3 Heat Flow Measurements

Heat flow measurements in the ESRP are based on calculations combining measured, or estimated, thermal conductivity and measured temperature gradients. Brott et al. (1976) conducted the first regional heat flow study of southern Idaho. Low heat fluxes (<50 mW/m^2) measured for the central part of the ESRP were obtained from shallow wells (<200 m [<656 ft]) and are not representative of the upward geothermal heat flux. As discussed previously, the low heat fluxes reflect masking of the regional heat flow by the fast-moving, cold water in the ESRP aquifer, which effectively transports the regional heat flux downgradient to groundwater discharge areas to the southwest of the INL Site (McLing et al., 2016). High heat flow values are well documented in the rock beneath the ESRP aquifer in deep holes. Brott et al. (1976) found anomalously high heat flow values (300 mW/m^2 or greater) on the borders of the SRP and noted that the anomalous regional heat flow pattern around the ESRP, together with other geophysical geological data, suggests the presence of a major crustal heat source. .

3.4 Heat Flow Map

The Southern Methodist University (SMU) Geothermal Laboratory (Blackwell et al., 1991) has generated heat flow maps of the United States (Figure 5) using temperature and thermal conductivity data now available in the National Geothermal Data System. Based on these maps, the area with the highest heat flow in the region is Yellowstone National Park (+150 mW/m^2). Vertical heat flow in the ESRP beneath the GRRA is 110 mW/m^2 and is among the highest heat flows in the country.

Heat flux data points in the SMU study were assigned a quality ranking based on the drilled depth and the quality of the data. Deeper wells received higher rankings, and, within the ESRP region, only wells deeper than 100 m (328 ft) were considered. The general ranking criteria are described by Blackwell et al. (1991). Data were contoured using a minimum curvature algorithm with a tension factor of 0.5, averaging all points within a 0.02 spacing of each other, and a grid interval of 1.52 m (5 ft) (0.08333°) of latitude/longitude. Points were added to constrain the contours to follow structural/province trends in areas of sparse data coverage.

3.5 Temperature Profile for Site

Blackwell et al. (1991) analyzed data from more than 35,000 sites to estimate temperature versus depth within the conterminous United States as a measure of EGS resource potential. Portions of the 3.5-km (11,483-ft) and 4.5-km (14,764-ft) depth maps around southeastern Idaho (Figure 6) illustrate the high temperatures at relatively shallow depths. The closest deep borehole to the GRRA is INEL-1. Extrapolation of temperature versus depth in the borehole, assuming a thermal conductivity varying one-third lower to one-third higher than the measured values to 3 km (9,843 ft), suggests that the temperature profile at that location may be similar to that depicted in Figure 7.

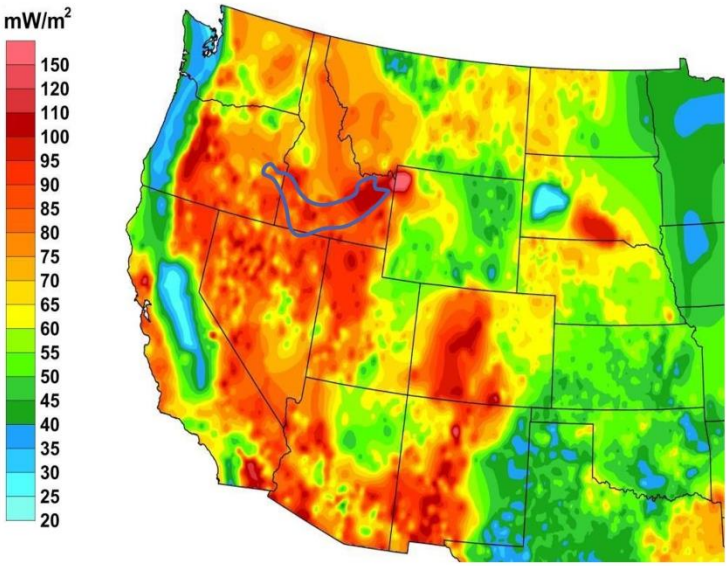

Figure 5. Heat flow map of the western United States (Blackwell et al., 1991) showing the location of the SRP.

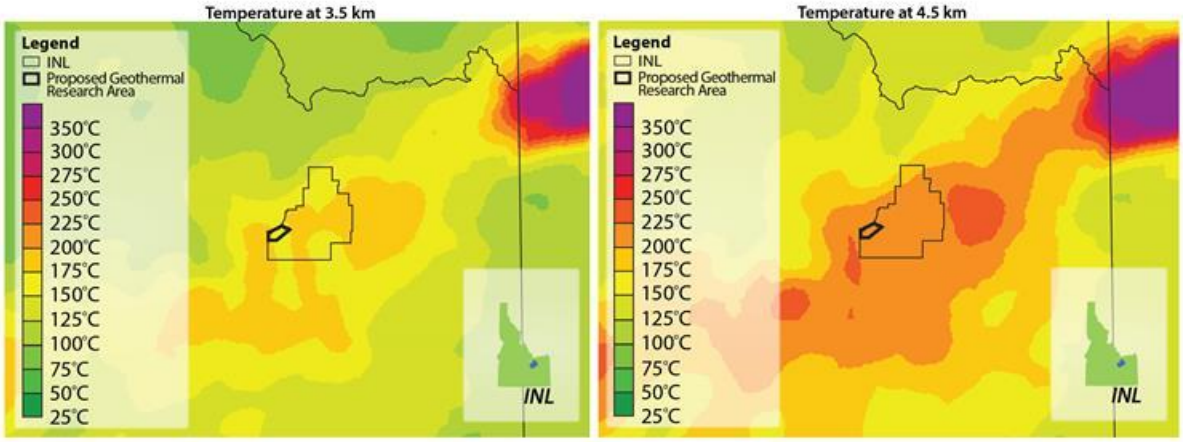

Figure 6. Temperature contour maps at different depths for southeastern Idaho (modified from Blackwell et al. [1991]). The INL Site and GRRA boundaries are shown with light and bold black lines, respectively.

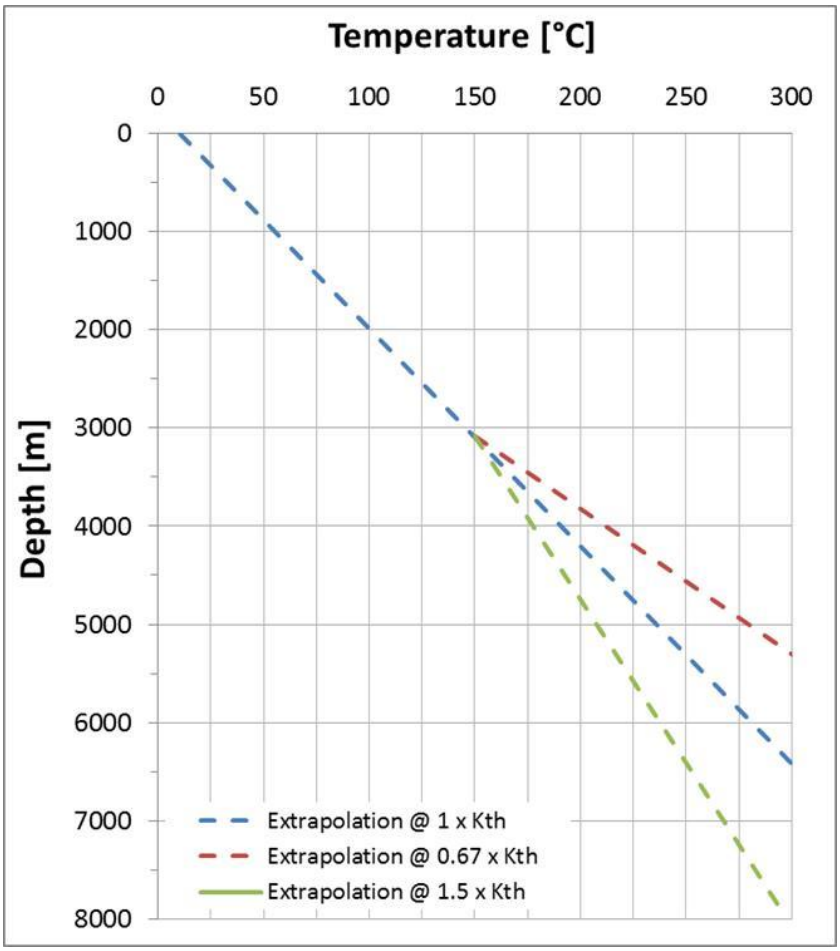

Figure 7. Temperature gradient of INEL-1 and extrapolation of its temperature gradient to greater depths assuming thermal conductivity of (a) 1 K_{th} and (b) 1.5 K_{th} and 0.67 K_{th} that was measured in the lower portion of INEL-1 (~3 w m^{-1} K^{-1}).

3.6 Heat Generation Mechanism

The ESRP thermal anomaly is a result of the passage of the North American Plate over the Yellowstone Hotspot. The Yellowstone Hotspot thinned the lithosphere and fueled the intrusion of hot basaltic magma into the lower and middle crust, forming a sill complex up to 10 km (6 mi) thick (Shervais et al., 2011). The onset of "hotspot"-related volcanism is generally marked by the eruption of large volumes of dry, high-temperature rhyolites and followed by up to 1 km (0.6 mi) of "post-hotspot" basalts (Shervais et al., 2013). Relatively recent MT studies suggest that the Yellowstone Hotspot may not represent a simple single shallow-magma plume. Kelbert and Egbert (2012) interpreted MT data as evidence of large volumes of partially molten rock extending westward underneath much of the ESRP, and these residual lenses of magma are the most probable sources of heat beneath the ESRP.

3.7 Thermal Conductivity as a Function of Depth

Thermal conductivity values as a function of depth for three deep boreholes in the ESRP are presented in Figure 8. The thermal conductivity value shows a significant increase in INEL-1 at a depth of 0.75 km (2,461 ft), and, at the total depth of the borehole, thermal conductivity is approximately 3.2 watts/(mK). Recently, the project hotspot boreholes were drilled to depths on the order of 2 km (6,562 ft), and thermal conductivity values will be available from the core from these wells.

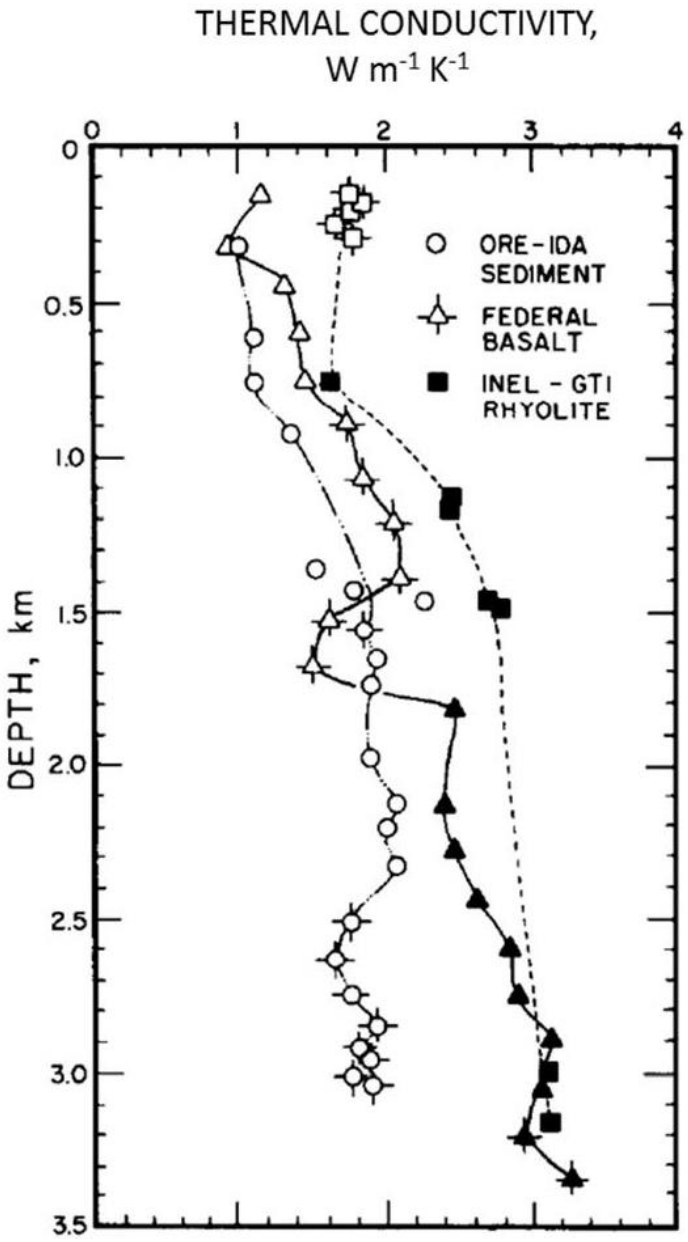

Figure 8. Thermal conductivity versus depth for three deep wells in the SRP (Blackwell, 1989).

3.8 *Geothermal Gradient

Vertical geothermal gradients for the ESRP are based on temperatures below the aquifer, because flow in the aquifer disturbs the shallow, vertical-temperature gradient. Temperature profiles in the deeper portions of the wells shown in Figure 4 generally display the characteristic break in slope at the bottom of the upper productive aquifer. Where sufficient temperature data exist to indicate the geothermal gradient at that location, those calculated gradients are summarized in Table 1 and plotted in Figure 9.

Combining data from these wells with ESRP geothermal gradients described by Blackwell (1989) (but excluding data deemed as unreliable by the authors) yields the range of values described in Table 1 and Figure 9. Of these wells, Kimama had the maximum gradient of 75°C/km (4.1°F/100 ft) and Well CH-1

had the lowest gradient (39°C/km [2.1°F/100 ft]), and the average temperature gradient of the data set is 54ºC/km (3.0°F/100 ft).

Table 1. Geothermal gradients measured in deep wells for this study and by others. Projected surface temperature and projected depths to reach 175 and 225°C (347 and 437°F) are also shown. Gradients for Sturm 1 and Anderson Camp wells are from Blackwell (1989).

Location	Gradient (°C/km)	Depth (km) to 175°C	Depth (km) to 225°C
INEL-1	44	3.8	5.0
W-02	77	2.6	3.3
CH-1	41	4.2	5.5
C1A	49	3.6	4.6
CH-2A	60	3.0	3.8
Sturm 1	48	3.5	4.5
Anderson Camp	63	2.6	3.4
Kimama	75	3.0	3.7

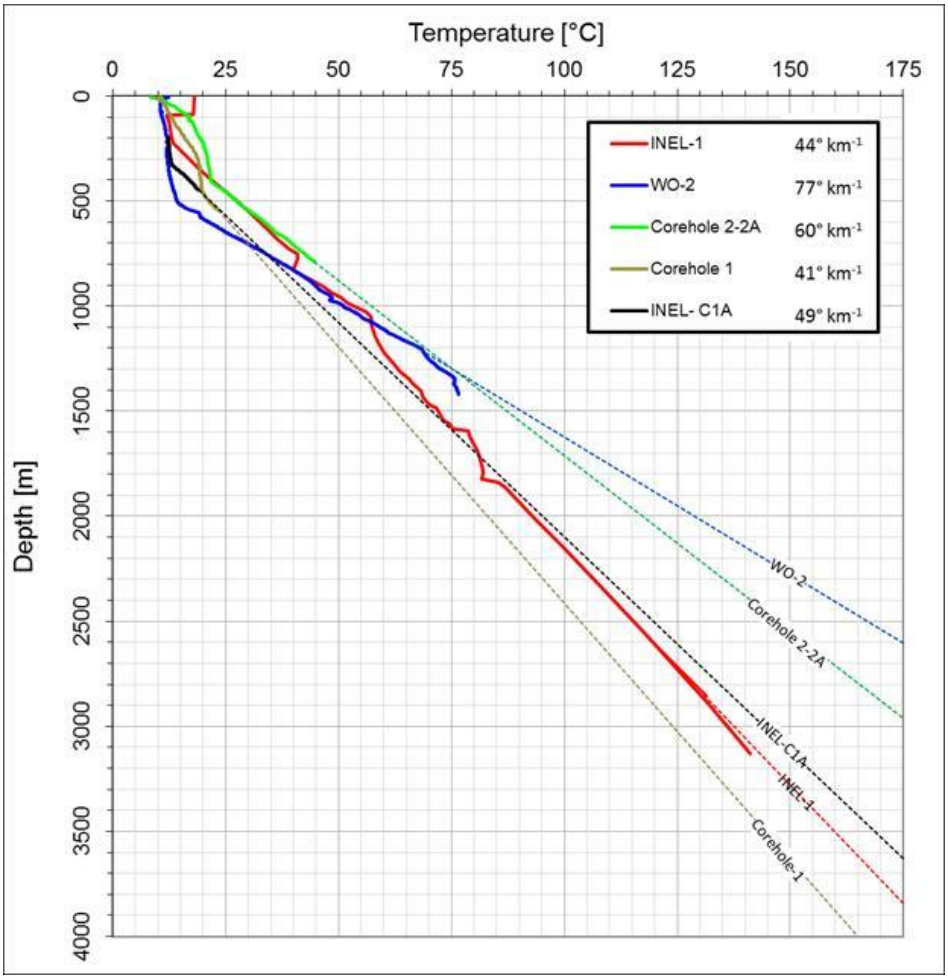

Figure 9. Temperature profiles (solid curves) from wells on the INL Site with sufficient depth below the aquifer to allow estimation of the local geothermal gradient. Dashed curves show extrapolations of calculated gradient to a temperature of 175°C (347°F).

3.9 Radioactivity of the Crustal Rocks

While radioactivity in crustal rocks in the ESRP region plays only a minor role as a source of heat, radioactive minerals can be a concern in the transfer of naturally occurring radioactive minerals from the subsurface to the surface by dissolution in the subsurface and subsequent precipitation in scale deposits at the surface. The mineral structure of rhyolites, like other silicic igneous and erupted volcanic rocks, can contain naturally occurring radioactive minerals in relatively low concentrations that can be a concern if anthropogenic processes lead to their concentration. The National Institute of Radiological Sciences, Research Center for Radiation Protection (Figure 10) indicates that potassium-40 typically provides greatest radioactivity in rhyolitic rocks, with activity of up to ~9,000 Bq/kg. No additional radioactivity data are available for the ESRP volcanic rocks.

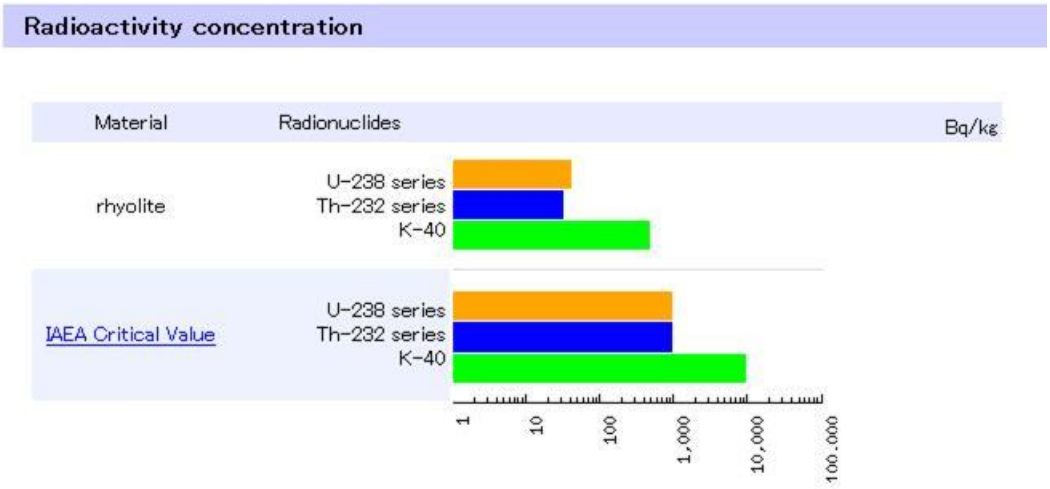

Figure 10. Mean radioactive mineral concentrations for rhyolite, as reported by the National Institute of Radiological Sciences, Research Center for Radiation Protection (NIRS, 2014).

3.10 Thickness of the Radioactive Layer

Volcanic tuffs and rhyolitic rocks are expected to extend from below the basalt to the target depths for EGS development, a thickness of several kilometers. Because boreholes have not penetrated the erupted volcanic units, total thickness is unknown.

4. RESERVOIR AND SUBSURFACE CHARACTERIZATION

The following sections describe the depth range of the target formation for our EGS reservoir and its associated properties.

4.1 *Depth to Resource

To estimate the depth to the zone where appropriate host rock has sufficient temperature for EGS development, we project the thermal gradients measured in the ESRP from the bottom of the aquifer, where heat transfer is dominated by the upward conductive heat flux. INEL-1 is the closest deep borehole to the proposed geothermal study area and provides a reasonable reference for the likely depth to reach geothermal target temperatures. Extrapolation of temperature data from INEL-1, with a temperature gradient of 44°C/km (111°F/100 ft) and a bottomhole temperature of 150°C (302°F) at 3,160 m (10,367 ft), indicates that a borehole would reach 175°C (347°F) at 3.8 km (12,467 ft). Depths to reach temperatures of 175 and 225°C (347 and 437°F) in other deep boreholes at the INL Site are given in Table 1 and plotted in Figure 9.

Temperature versus depth data in the GRRA can also be inferred from Blackwell's 2011 contour maps at varying depth (Figure 6). Based on those maps, temperature at a depth of 3.5 km (11,483 ft) will exceed 175°C (347°F).

Based on pressure data from deep wells in the area, hydraulic potential at the proposed FORGE site is likely to be close to a hydrostatic condition. Thus, if the depth to the water table is similar to that at INEL-1 (~180 m [~590 ft]), the fluid pressure at the deepest estimated resource depth of 3.8 km (12,467 ft) would be approximately 36.2 MPa.

While there are no deep boreholes within the GRRA to provide a direct measure of temperature gradient therein, groundwater temperatures in the study area (Figure 3) are significantly higher than typical aquifer temperatures, suggesting that the aquifer has little influence on the vertical heat flux (McLing et al., 2016) in that area, and that vertical heat fluxes in that area are higher than those below the aquifer, likely reflecting resurgence of deep circulating meteoric water.

4.2 Reservoir Planar Area

The planar area of the regional geothermal reservoir is roughly coincident with the area of the ESRP aquifer, approximately 26,000 km^2 (10,039 mi^2). The area of the reservoir within the GRRA is 100 km^2 (39 mi^2). The conceptual model of the deep reservoir is that elevated temperatures will be distributed over the entire GRRA. Local areas with elevated temperatures may be present, as suggested by MT data. Phase 1 research will resolve the best areas within the GRRA area to focus drilling.

4.3 Stratigraphy/Stratigraphic Columns

The stratigraphy of the FORGE site is anticipated to be similar to that encountered in the INEL-1 borehole (Figure 11). As described by Mann (1986), at the INEL-1 drill site, highly fractured basalt rocks occurred from land surface to a depth of 658 m (2,160 ft). In this sequence, four sedimentary interbeds were penetrated ranging from a few feet to up to 36 m (120 ft) thick. Between 658 and 742 m (2,160 and 2,435 ft), tuffaceous interbeds were penetrated and sometimes showed a calcareous and silty claystone. From 742 to 2,463 m (2,435 to 8,080 ft), the material penetrated mainly consisted of welded rhyolite tuff with several 6- to 12-m (20- to 40-ft)-thick tuffaceous interbeds. And from 2,463 to 3,159 m (8,080 to 10,365 ft), the test hole penetrated a hydrothermally altered rhyodacite ash flow.

4.4 *Lithology

The lithology of INEL-1 consists of 600 m (1,968 ft) of basalt underlain by 50 m (164 ft) of sedimentary interbeds underlain, in turn, by >2,500 m (8,202 ft) of rhyolite ash, ash flow tuff, and possible hypabyssal intrusive rocks (Lanphere, et al., 1994; Leeman et al., 2009). Lithologies in other wells are generally volcanic rocks of rhyolitic and basaltic composition and, less often, lacustrine sedimentary rocks.

Basalts of the ESRP are dominantly olivine tholeiites consisting of approximately 50 to 60% labradorite, 40% augite, less than 10% olivine, and 5% glass (Morgan et al., 1984). Iron-titanium oxides (mostly magnetite) and minor apatite also occur. The basalts are typically porphyritic, consisting of phenocrysts of olivine and plagioclase in a fine-grained matrix of interlocking plagioclase, augite, Fe-Ti oxide minerals, and intersertal tachylitic glass (Bates, 1999; Knutson et al., 1990; Kuntz et al., 1992; Lanphere et al. 1993). Flow margins are generally highly vesicular, and large parts of flows are characterized by abundant diktytaxitic cavities (Bates, 1999). Upper and lower flow contacts often contain coarse basalt rubble with high hydraulic conductivity.

The rhyolitic rocks, which make up the deep geothermal target area, are compositionally similar to SiO_2 ranging from 71 to 76% (Lanphere et al., 1994). The phenocryst assemblage, including sanidine, plagioclase, quartz, magnetite, ilmenite, pigeonite, augite, orthopyroxene, with accessory zircon and apatite, indicates that the rhyolites were anhydrous at the time of their emplacement.

Post-emplacement alteration of the deep basalts and rhyolites has played a large role in the current hydrologic, mineralogical, and chemical composition of the deep volcanic rocks. The abundance of authigenic minerals filling fractures, vesicles, cavities, and other conductive structure increases significantly with depth (Leeman et al., 2009).

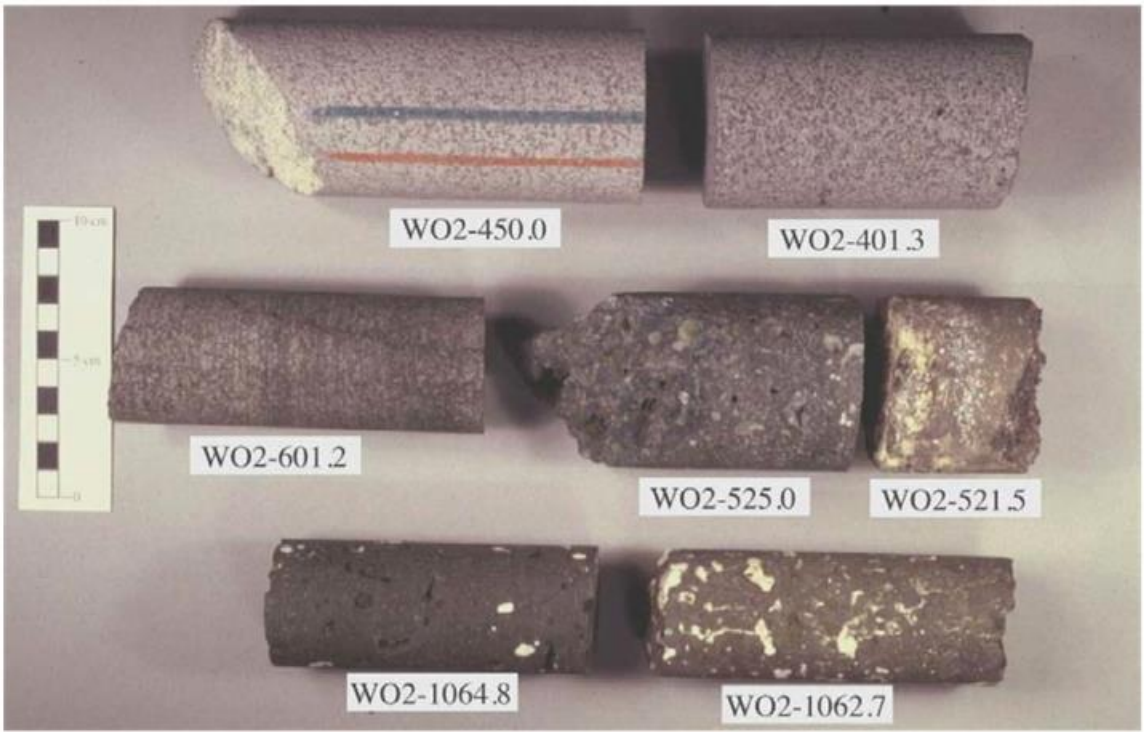

Figure 11. Photograph of W-02 core section (basalt and rhyolite) (Morse, 2002) showing the increased alteration of the deep rocks with depth. The severe alteration begins in the deep basaltic rocks and becomes more complete as the core transitions to rhyolite. Typical mineral assemblages for the altered ESRP rocks are calcite + smectite + zeolite.

4.5 *Stress State

Acoustic wellbore image data from four wells, including the deep INEL-1 borehole were analyzed in June 1990 to determine the state of stress beneath the eastern portion of the SRP. Limited data at that time precluded determination of the absolute stress magnitudes at the site; however, the study indicates that the proposed FORGE site is within a region of normal faulting (Sv > SHmax > Shmin).

A recent reanalysis of these data utilized associated geophysical well log data, drilling data, and newly acquired rock strength measurements (Bakshi et al., 2016) to fully constrain the in situ stress magnitudes at the site. In situ stress gradients at 3,353 m (11,000 ft) are Sv = 1.04 psi/ft, SHmax = 0.98 psi/ft Shmin = 0.74 psi/ft. Pore pressure is sub-hydrostatic at 0.43 psi/ft. Figure 12 shows the results of s preliminary geomechanical model for INEL-1.

In situ stress orientation indicators such as wellbore breakouts and drilling-induced tensile wall fractures were not observed in the original 1990 image logging program, precluding measurement of in situ stress orientation from these data. Although drilling-induced tensile wall fractures would be expected to occur at depth in the deeper INEL-1 borehole, it is likely that the relatively low-resolution circa-1990 acoustic televiewer tool could not resolve these fine-scale features. It is strongly recommended that more contemporary, higher-resolution wellbore image logging be undertaken at the FORGE site as part of the next Phase 2 logging program.

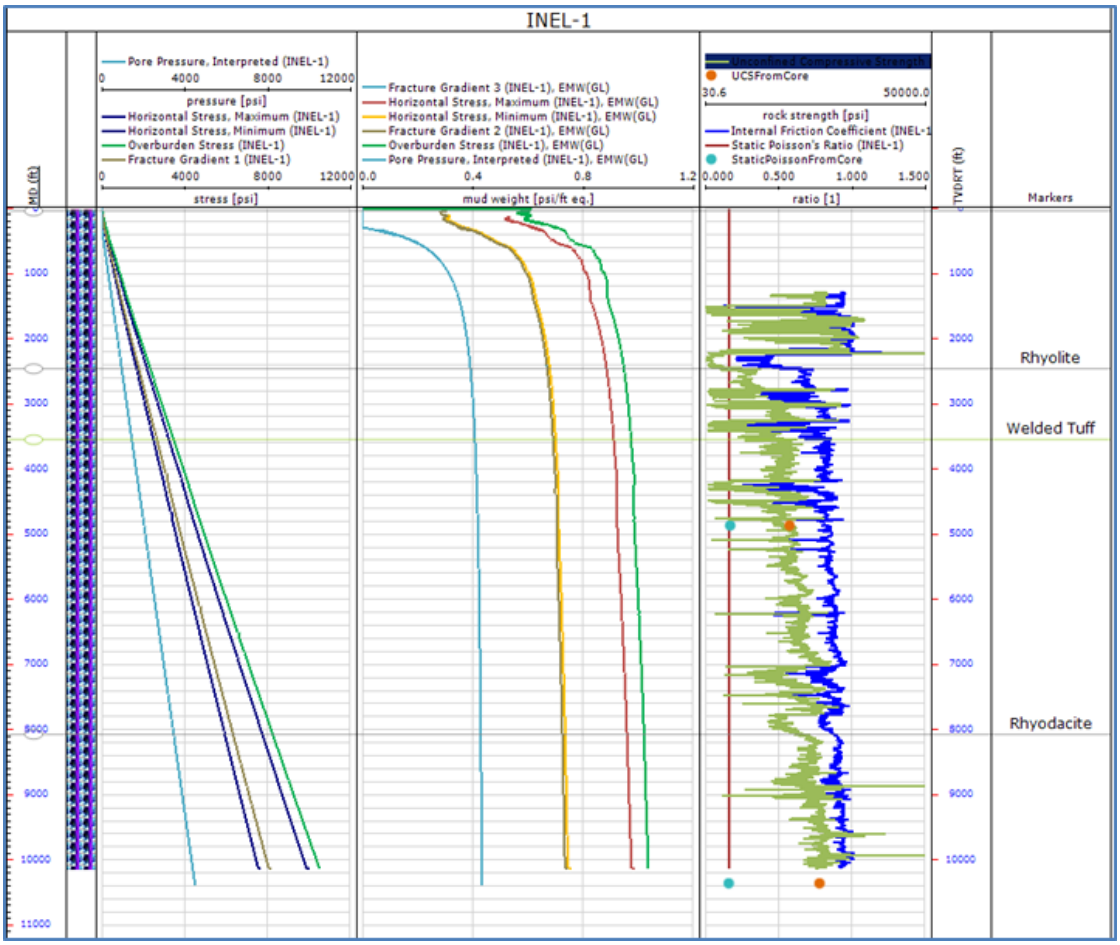

Figure 12. Geomechanical model of the FORGE site permeability data.

Several hydraulic tests were conducted in INEL-1 (Mann, 1986), with the deepest between the interval from 1.3 km (4,265 ft) to 3.2 km (10,499 ft) below ground surface. The open hole was pumped for 7 days. The average reservoir permeability for the interval was calculated as 7.2×10^{-16} m^2. More recently, core samples from another deep borehole on the INL Site, W-02, were analyzed by the project team for mechanical and reservoir properties in 2014. These 2.5-cm (1-in.)-diameter core samples from approximately 1,340 m (4,400 ft) below ground surface were measured to have an air permeability less than 2×10^{-18} m^2 at 27.6 MPa (4,000 psi) confining stress with porosity ranges from 3 to 15%. These low permeability values from the laboratory core tests as compared to the field test results (approximately 100 times less permeable) suggest that fractures may be controlling the permeability in the field.

4.6 Existing Features

Volcanic rifts within the SRP are discernible as linear arrangements of volcanic landforms and structures, including noneruptive fissures, faults, and grabens. These volcanic rifts are oriented northwest-southeast, perpendicular axis of the SRP and are characterized by extensional tectonics; elevated heat flux and geothermal features; linear trends with volcanic vents; and faults and cracks associated with the motion and emplacement of volcanic dikes that may or may not reach the surface. The Axial Volcanic High is a volcanic center oriented north-south along the axis of the ESRP. These features are shown in Figure 13.

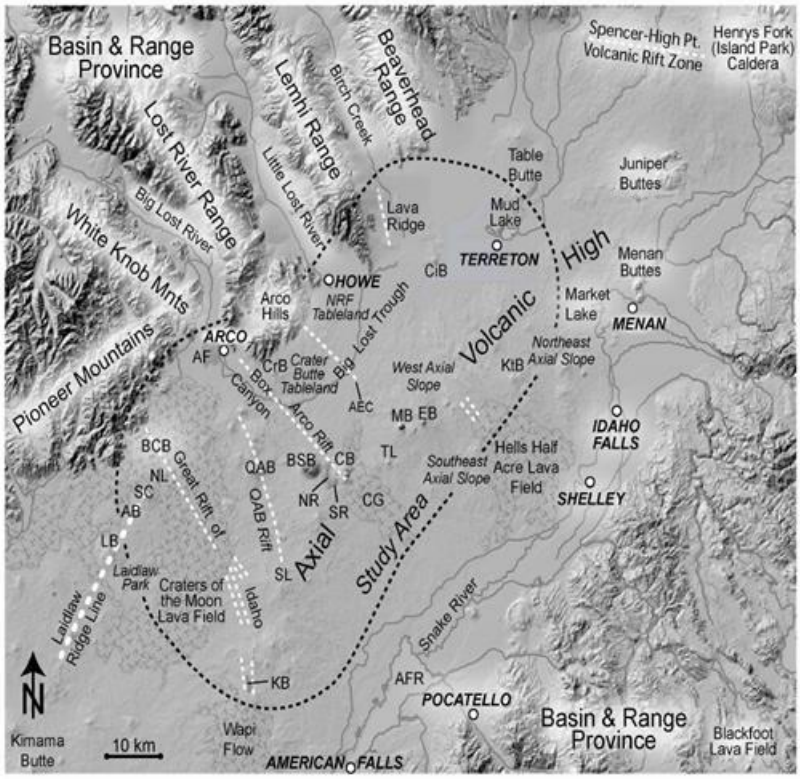

Figure 13. Geographical and geological features in the greater study area of the INL Site. Lava fields less than 15,000 years old are denoted by the mottled background pattern. The approximate trends of volcanic rift zones are shown as dashed white lines (Stanley, 1982).

4.6.1 Fracture Location

The best source of fracture distribution is the 1990 borehole televiewer logging data of Moos and Barton (1990) for the INEL-1 borehole. That analysis, which examined the interval between 2,067 and 3,123 m (6,781 and 10,246 ft), was performed to examine the stress state of the ESRP, via borehole breakout data, and to determine fracture distribution and characteristics. A total of 2,568 orientations and 2,273 apertures measurements were determined from the televiewer data, including fracture orientations and apertures for fractures with apertures between 5 and 500 mm (0.2 and 19.7 in.) and orientations for those as well as smaller fractures for which apertures could not be measured.

No breakouts were identified in the 1990 televiewer data, as was also the case with the original 1980 televiewer logs. This suggests a normal faulting stress regime with a hydrostatic or incipient faulting stress regime (Moos and Barton, 1990).

4.6.2 Fracture Orientation

A stereographic projection indicating fracture strike and dip of mapped fractures in INEL-1 is displayed as Figure 14 (Moos and Barton, 1990). A significant (statistically) concentration of fracture orientations strikes east-northeast (~azimuth = 75 degrees) and dips steeply to the northwest (~78 degrees). A secondary population is subhorizontal, with dips from 5 to 30 degrees. Moos and Barton (1990) suggest that the large number of near-vertical fractures, and their preferred orientation, indicate a common origin, possibly reflecting intense fracturing associated with caldera collapse, a hypothesis supported by the preponderance of fracture infilling.

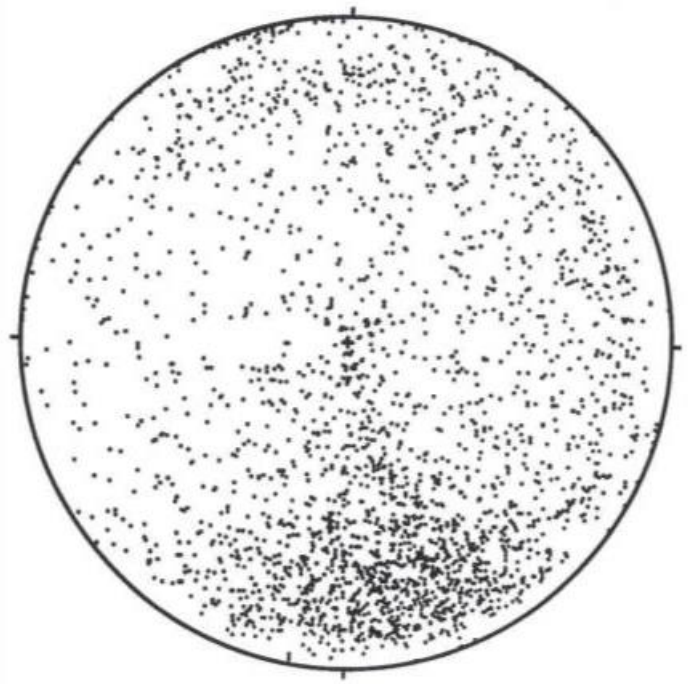

Figure 14. Lower-hemisphere, stereographic projection of orientations of poles to fracture planes identified in Borehole INEL-1 between 2,067- and 3,123-m (6,781- and 10,246-ft) depth. Figure from Moos and Barton (1990).

4.6.3 Fracture Aperture

Relative fracture apertures (Moos and Barton, 1990) are indicated in tadpole plots of fracture dip and dip direction in Figure 15. Those data indicate that larger fractures have steeper dip than smaller fractures, and that these larger fractures are dominant in the concentration of fractures showing a distinct east-northeast trend with northwest dip. Reactivation of the fractures with the dominant observed orientation would require at least horizontal stress oriented perpendicular to the axis of the plain.

4.7 Existing Faults (Location, Proximity, Activity)

The closest mapped Quaternary faults are the northwest-trending, southwest-dipping Lemhi and Lost River range-bounding normal faults. Paleoseismic data indicate the most recent offsets occurred 15,000 to 25,000 years ago along the southernmost fault segments, which are the closest to the GRRA (Woodward-Clyde, 1992; Wood et al., 2007). The surface scarp of the Lemhi southernmost fault segment is located 19 km (12 mi) north of the GRRA. Cross faults mapped in the footwall and expressed in the subsurface of gravity data of the southernmost end of the Lemhi fault are thought to have accommodated offsets over the past 4 million years (Woodward-Clyde, 1995). The end of the southernmost fault segment of the Lost River fault is located 19 km (12 mi) to the south of the GRRA. Geophysical studies conducted in this area suggest the presence of possible northeast-trending normal faults at the boundary of the ESRP and Basin and Range (Bruhn et al, 1992; Hadley and Cavit, 1984).

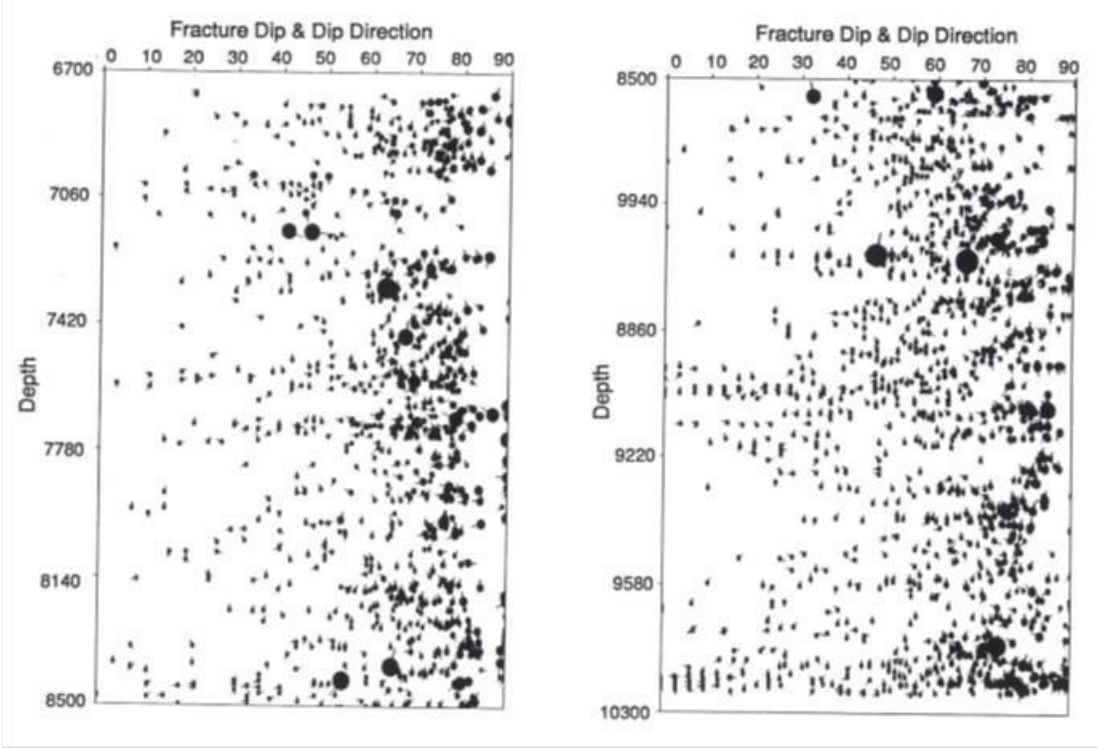

Figure 15. Tadpole plot of fracture orientation (abscissa) versus depth (ordinate) for the INEL-1 borehole. Dip direction is indicated by compass angle of the tadpole tail; symbol size indicates relative fracture aperture. Figure from Moos and Barton (1990).

The northern part of the GRRA is also located within the Howe-East Butte volcanic rift zone. Northwest-trending small normal faults or fractures may be present in the subsurface, which may be covered by subsequent younger lava flows. Basalt dike intrusion within this volcanic rift zone occurred during the Pleistocene (~230,000 to 730,000 years ago) (Hadley and Cavit, 1984). Dike intrusion causes incremental near-surface and surface deformation, which produces new short fractures or faults (Hackett et al., 2002). Dikes tend to propagate at shallow levels (<4 km [<2.5 mi]), and the associated extensional structures are correspondingly shallow (Payne et al., 2008). The Arco Volcanic Rift Zone, 18 km (11 mi) south of the GRRA, has short normal faults, fissures, and fractures attributed to dike intrusion (Du and Aydin, 1992).

4.8 *Lithology Logs

The deepest borehole located along the northern boundary of the GRRA is USGS-142. In this borehole, the contact between basalt and underlying rhyolite was encountered at a depth of 425 m (1,394 ft), and rhyolite extended to the bottom of the hole at 579 m (1,900 ft). A lithology log for USGS-142 is provided as Figure 16. The deepest lithologic log near the GRRA is from INEL-1 (Figure 17). A number of deep boreholes exist on the INL Site, including WO-2 and Well 2-2A, and a summary of selected lithologic characteristics and possible correlations of rock units in those boreholes is provided as Figure 18.

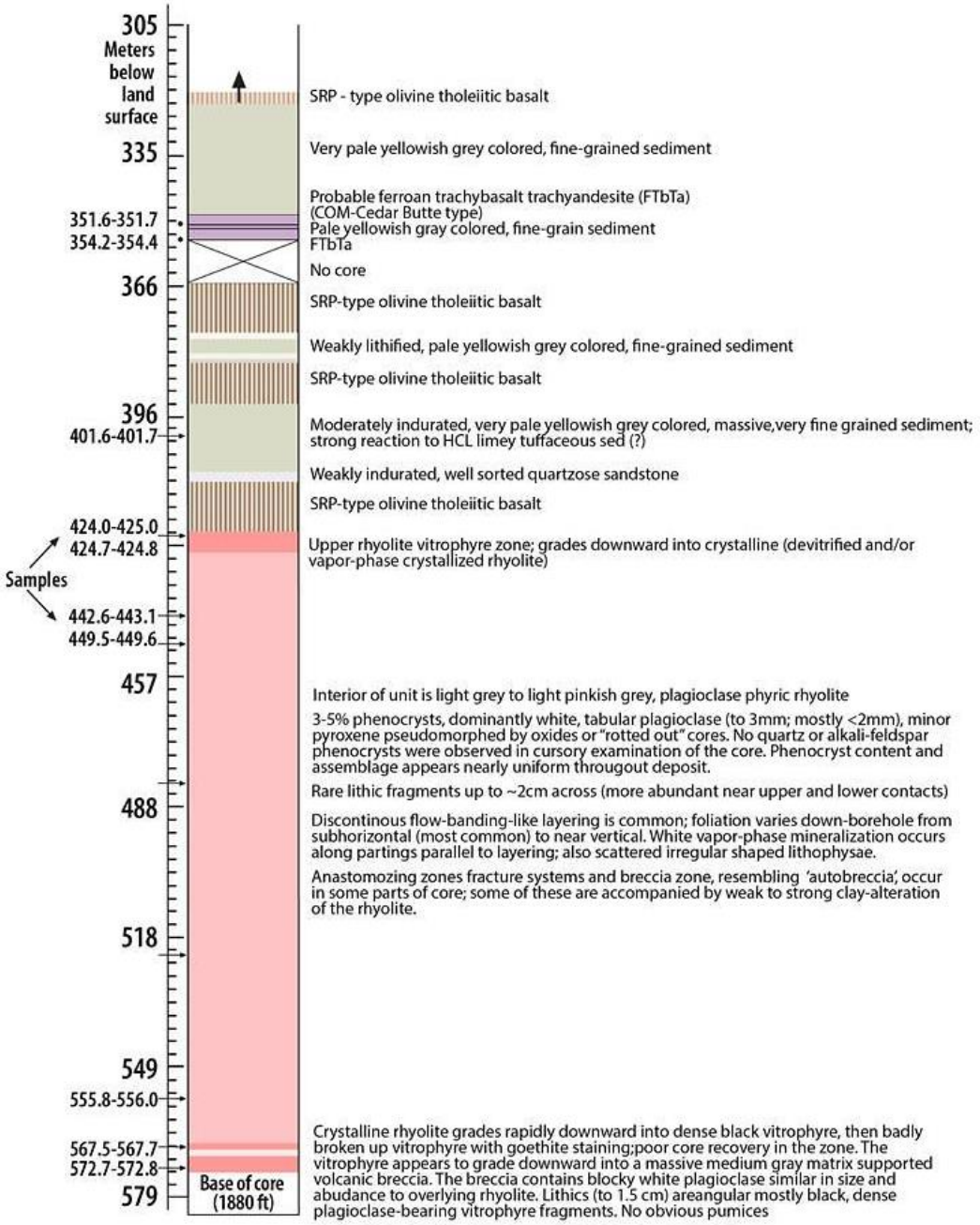

Figure 16. Lithology log of USGS-142, located within the GRRA.

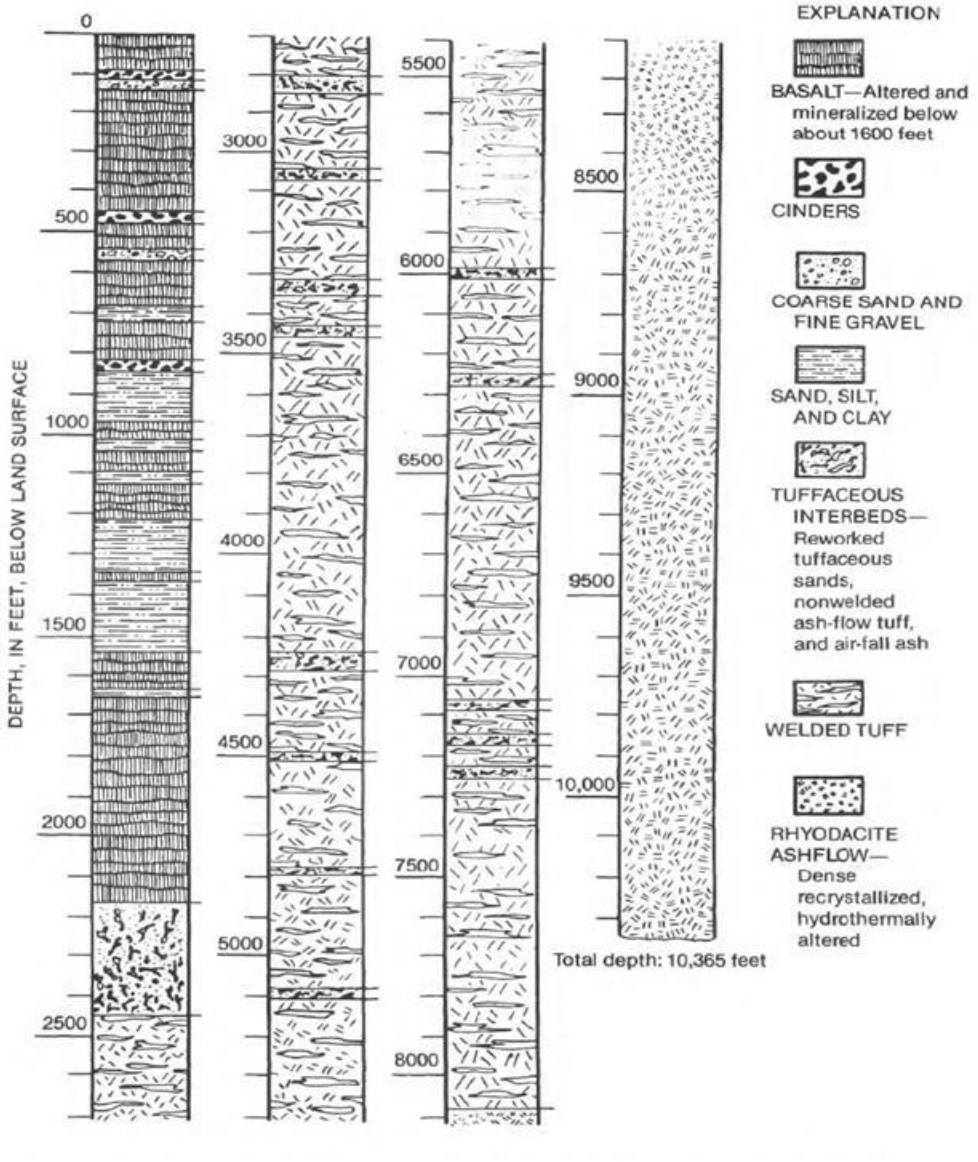

Figure 17. Generalized lithologic log of rock units penetrated by INEL-1 test hole (Mann, 1986).

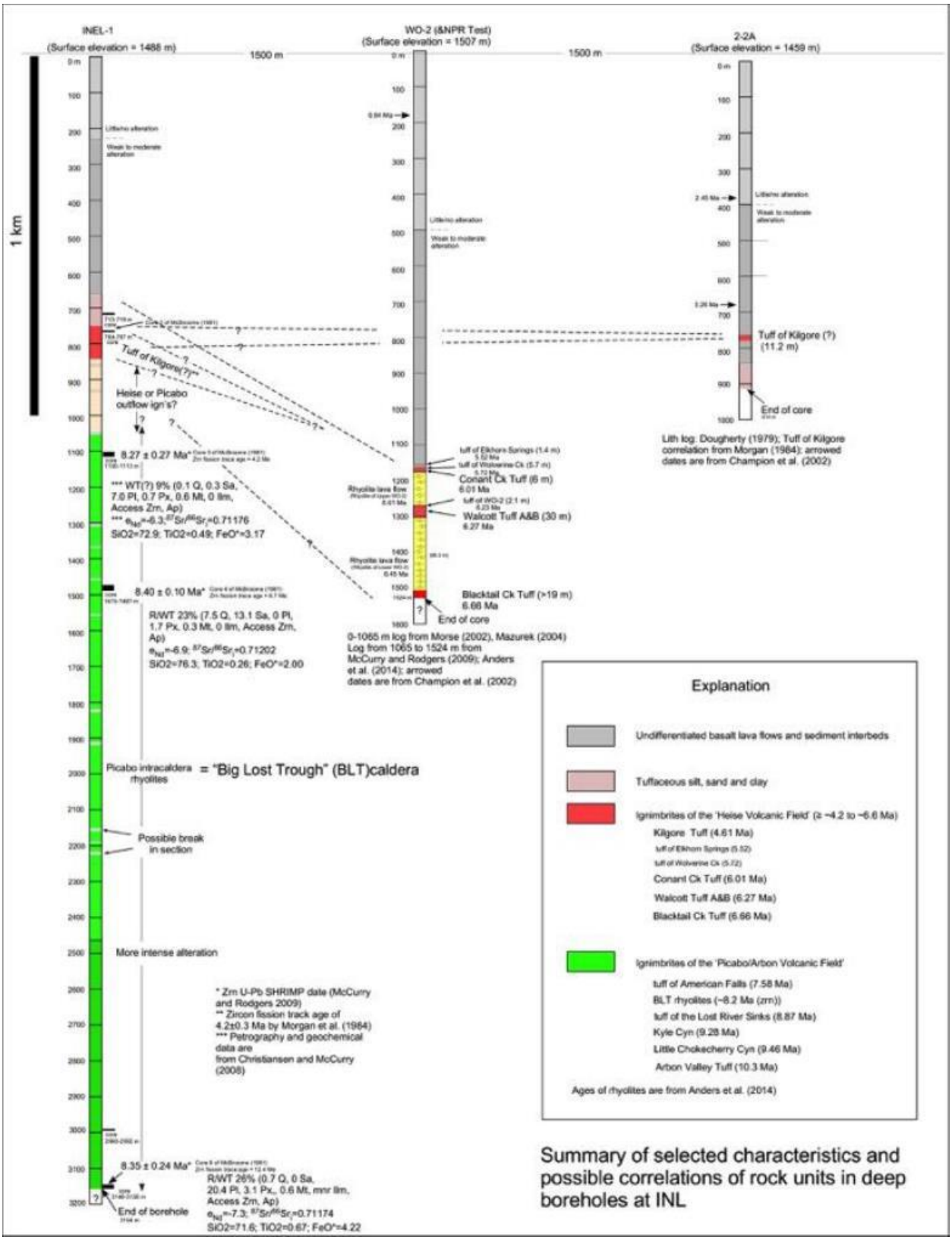

Figure 18. Summary of selected characteristics and possible correlations of rock units in deep boreholes at the INL Site.

4.9 Subsurface Data

4.9.1 Gravity Data

Regional and detailed gravity surveys have been conducted in the ESRP and adjacent Basin and Range. Early regional gravity studies were conducted to assess the compositions of the ESRP crust relative to the surrounding Basin and Range crust (Smith et al., 1996). Additional detailed gravity studies were performed to assess possible boundary faults near the southernmost ends of the Lost River and Lemhi ranges (Bruhn et al, 1992). More recent compilations of gravity data and processing have produced Bouguer, isostatic residual, vertical derivative, intermediate-wavelength, long-wave length, and maximum horizontal gradient maps of the ESRP (Mabey, 1982). These data, along with aeromagnetic data, have been used to delineate deep-seated crustal structures to assess controls on regional fluid flow (Hildenbrand et al., 2000). The gravity and aeromagnetic data for the ESRP are available at the Pan American Center for Earth and Environmental Studies at the University of Texas at El Paso.

4.9.2 Magnetotelluric (MT) Surveys

About 1980, two MT surveys were conducted along transects across the SRP by the United States Geological Survey (USGS) (Pankratz and Ackermann, 1982). The first, at a semi-regional scale, spans from the Raft River geothermal system northeastward into Yellowstone National Park. Near the surface, it suggests that up to 2 km (1.2 mi) of resistive basalt flows overlay a similar thickness of relatively conductive lacustrine sediments and altered rhyolite flows. Below these units are generally high-resistivity materials, denoting an igneous basement complex and granitic crust to depths of 15 to 20 km (9 to 12 mi). Underlying the high-resistivity unit is an inferred deeper crust of very low resistivity (<5 ohm-m). The low-resistivity layer likely corresponds to broad zones of similar resistivity that underlie much of the active extensional Great Basin area where mafic underplating, magmatic hybridization, and hydrothermal fluid release constitute substantial concentrations of high-temperature conductive fluids and melts (Hildenbrand et al., 2000). The lower crustal conductive region rises to depths as shallow as ~5 km (3 mi) under the Yellowstone magmatic-hydrothermal system. The second MT profile, of Stanley et al. (1982), includes higher resolution sampling and extends a length of ~30 km (19 mi). It trends northwest to southeast through Borehole INEL-1 and the proposed FORGE location. Results indicate a thin layer (~250 m [820 ft]) of resistive Quaternary basalts overlying ~1,500 m (~4,921 ft) of mixed sediments and altered tuffs, all underlain by resistive, unaltered volcanics. As seen in the first study, a similar crustal layer of high resistivity extends to depths of 15 to 20 km (9 to 12 mi), which is underlain by the low-resistivity, deep crustal unit.

Recently, the Earthscope MT survey and interpretations by Kelbert and Egbert (2012) and Meqbel et al. (2014) have added to the general understanding of the deep subsurface. The Earthscope MT stations recorded only relatively lower frequency data and were spaced on average 70 km (43 mi) apart (Figure 19), with a more dense profile running northwest-southeast across the SRP near the INL Site (Kelbert and Egbert, 2012). The three-dimensional inversion models of these surveys indicate a generally resistive upper crust under the SRP, with lower crustal resistivity falling at greater depths to a minimum just below the Moho. Processes of magmatic underplating and fluid release were inferred to explain the deep low (Wannamaker et al., 2008). Very striking in the images of Kelbert and Egbert (2012) are numerous low-resistivity upwellings around the margins of the SRP, including in the INL Site vicinity. These structures are interpreted to represent, at least in part, geothermal fluids formed magmatically near the margins of the plain by structurally dilatant conditions. The extensional conditions are thought to be set up by the movement of the ESRP as a coherent whole in a relative west-southwest direction (Stickney and Bartholomew, 1987). Regional shear is right-lateral along the northern plain margin and left-lateral along the southern plain margin. Apart from the regional hydrothermal significance of these structures, high-temperature fluids may be transported along these extensional zones and impart heat to the host rocks, potentially creating large prospects for EGS.

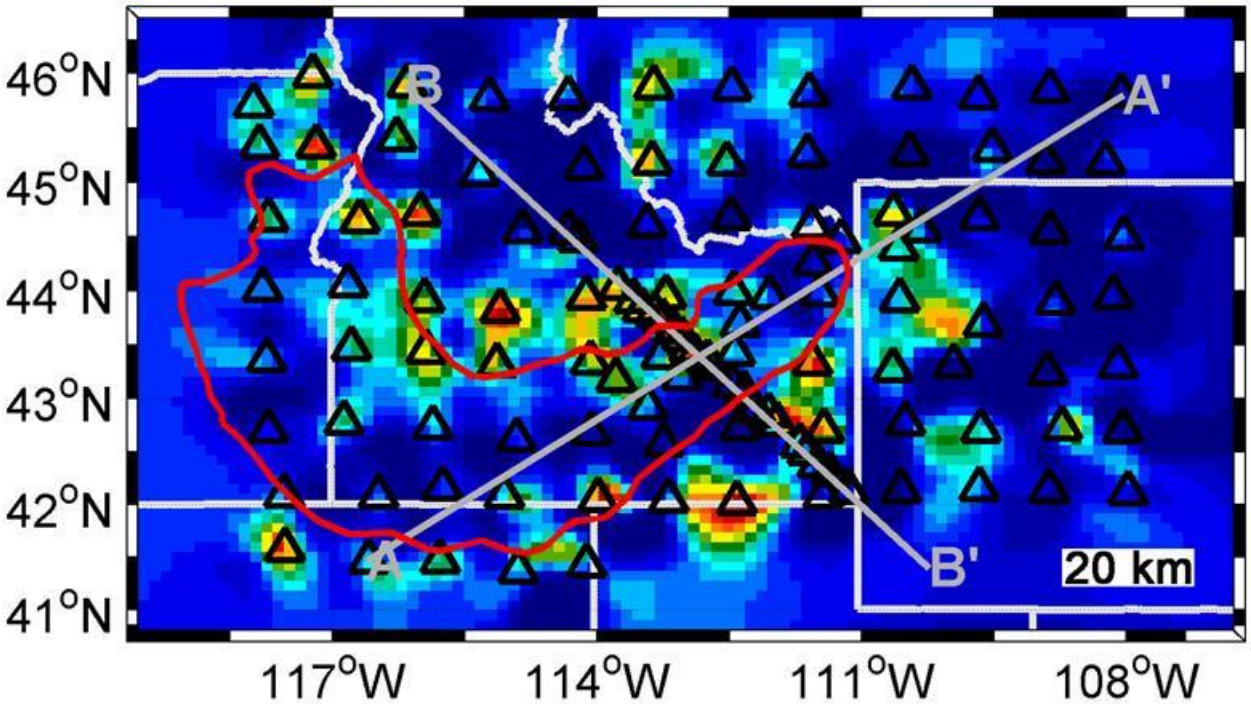

Figure 19. MT inversion model at a depth of 20 km (12 mi) for the SRP. Darker colors indicate increasing resistance (ohm-meters). The contours of the SRP are plotted in red for Knutson et al. (1990).

4.9.3 Seismic Reflection

Jackson et al. (2006) conducted seismic reflection studies in the ESRP (Figure 20) to determine the possible locations of the Lost River and Lemhi fault terminations. Thirteen seismic reflection lines were processed and interpreted:

- Four commercial seismic reflection lines shot using a Vibroseis source, located in the basins adjacent to the Arco segment of the Lost River fault and the Howe segment of Lemhi fault
- Seven lines acquired by EG&G Idaho Inc. Geosciences using multiple impacts with an accelerated weight drop source, located near the projected southern extensions of the Arco and Howe segments into the ESRP
- Two seismic lines shot by Sierra Geophysics in 1984 using an accelerated weight drop source, located near the projected southern extensions of the Arco and Howe segments into the ESRP.

This study concluded that the southern termination of the Howe segment is 2.2 km (1.4 mi) south of the fault's southernmost surface expression, and that within the basin, south-dipping normal faults at the northern end of Howe Line 81-3 and two southwest-dipping normal faults at the northeastern end of Howe Line 82-2 can be correlated with the Howe fault segment. South of the surface expression of the fault, Jackson et al. (2006) found that southwest-dipping normal faults on Howe Line H1 can be correlated with the Howe segment and that, further south, Howe Lines H2, H3, and S4 show continuous flat-lying reflectors and indicate no fault offset. The southern termination for the Howe segment was placed between Howe Lines H1 and H2.

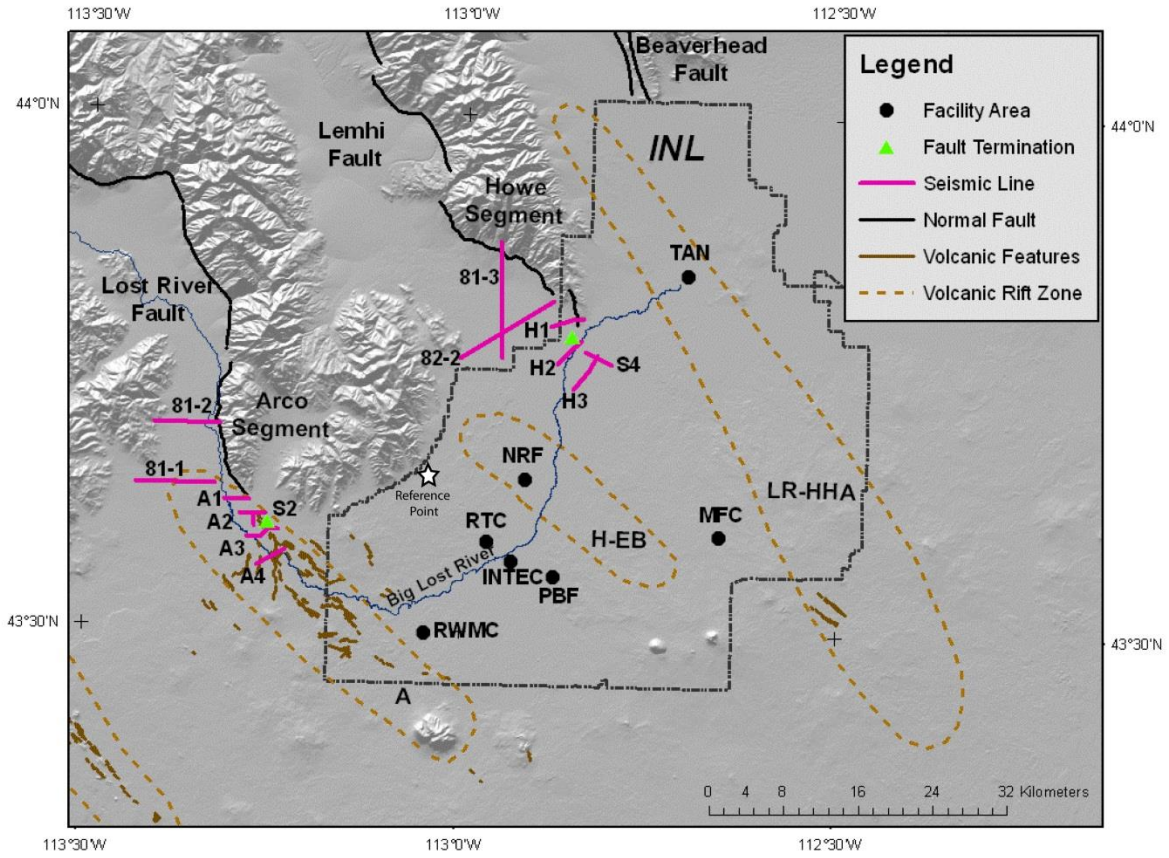

Figure 20. Map showing the locations of the seismic reflection lines relative to the normal faults and volcanic rift zones. The facility areas at the INL Site include the Materials and Fuels Complex (MFC), Power Burst Facility (PBF), Reactor Technology Complex (RTC), Idaho Nuclear Technology and Engineering Center (INTEC), Radioactive Waste Management Complex (RWMC), Naval Reactor Facility (NRF), and Test Area North (TAN).

4.9.4 Resistivity

The USGS conducted a deep resistivity survey in 1978 to study geothermal potential at the INL Site (Zohdy and Bisdorf, 1980). The survey consisted of Schlumberger soundings over an area of ~600 km^2 (232 mi^2) that overlaps the proposed project site and includes the area around INEL-1. Soundings indicated the presence of six primary geoelectric units. Units below the basalts were described as silicic volcanic rocks with thickness between 500 and 2,000 m (1,640 and 6,562 ft) underlain by a highly resistive layer interpreted as pre-Tertiary basement rocks extending to approximately 5-km (3-mi) depth.

4.10 Geochemistry

Since the establishment of the INL Site in 1949 (initially as the National Reactor Testing Station), there has been a concerted effort by the USGS and INL researchers to gather and interpret geologic, geochemical, geophysical, geothermal, and other related data for the region. During the past 70 years, countless studies have been conducted to support this mission, and the resulting data have been published and archived to support research projects such as FORGE. The data are of high value, representing an investment of tens of millions of dollars' worth of research and characterization for not only INL but for the ESRP as a whole. The ability to leverage seven decades of targeted research to applications such as

advanced EGS is unique to U.S. Department of Energy reservations like the 2,300-km^2 (890-mi^2) INL Site.

4.10.1 Geothermometry

To look for evidence of hidden hydrothermal reservoirs in the ESRP, Neupane et al. (1980) used INL's multicomponent equilibrium geothermometry program, RTEst, as well as traditional geothermometers to estimate source water temperatures of wells and shallow springs from along the margin of the ESRP (Figure 21). The source temperatures estimated using RTEst had means and standard errors of 118 ± 5°C (244 ± 41°F), 104 ± 15°C (219 ± 59°F), 91 ± 11°C (196 ± 52°F), and 79 ± 18°C (174 ± 64°F) for the Na-HCO_3, Na-HCO_3-Cl, Ca-HCO_3 and Ca-SO_4 water types, respectively. The standard error of 5°C (41°F) associated with the mean temperature of 118°C (244°F) for the Na-HCO_3 waters is smaller than typically observed for the individual RTEst optimized temperatures (~8°C [46°F]), indicating that these waters have little intra-type variation. This low variation suggests that the Na-HCO_3 waters have similar geochemical histories even though their locations are widely distributed across the ESRP (Figure 21). These Na-HCO_3 waters may have equilibrated with basalt flows below but near the base of the ESRP aquifer, possibly obscuring higher temperatures in the deeper rhyolite sections. The other water types exhibited lower mean temperatures and much larger standard errors (11 to 18°C [52 to 64°F]), indicating that these waters have much greater intra-type variations that likely reflect more complex thermal interactions in multiple geologic settings, leading to multiple geochemical histories. Estimated temperatures do not necessary indicate the maximum temperature of the geothermal resource that potentially could be exploited using enhanced drilling and fracturing technologies (e.g., EGS) but rather the permeable zone of a reservoir at which the water is in equilibrium with the assemblage minerals.

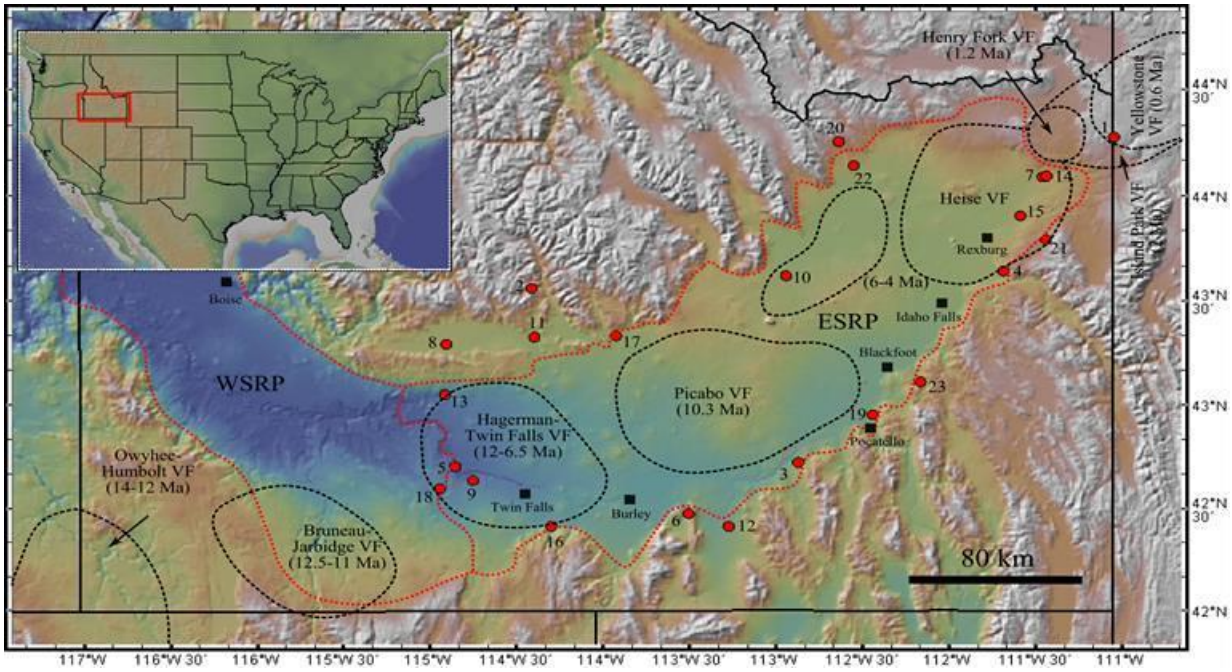

Figure 21. Shaded relief map of southern Idaho showing the SRP prepared from NASA 10-m digital elevation model data in GeoMapApp. The dotted red lines represent the boundary of the SRP. The ESRP is separated from the western SRP by stretches of the Snake River and Salmon Falls Creek (delineated by the north-south-trending dotted line west of Twin Falls). Areas within black-dashed polygons represent the super volcanic fields (VFs) (modified after Link et al. [2005]). The red dots represent locations of springs or wells in the ESRP and its margins that are used for temperature estimation. The number assigned to each spring/well corresponds to the case number given in Table 2.

Table 2. Preliminary temperature estimates for the ESRP reservoir using RTEst, silica polymorphs, and Na-K-Ca geothermometers (T in ºC).

Case No.	Spring/Well[a]	Field T	RTEst T (±σ[b])	Fournier (1979)		Arnorsson (1983) (25-180 ºC)	Fournier and Truesdell (1973)[d]	Water Type
				Quartz NSL[c] T	Chalcedony T	Silica T	Na-K-Ca T	
1	Boundary Creek HS	92	154±5	183	163	157	158	Na-HCO_3-Cl
2	Clarendon HS	47	127±6	125	97	97	114	Na-HCO_3-Cl
3	Indian WS	32	54±5	63	31	35	67	Na-HCO_3-Cl
4	Heise HS	49	76±10	79	48	51	123	Na-HCO_3-Cl
5	Salmon Falls HS	70.5	113±5	131	103	102	88	Na-HCO_3-Cl
6	SKGGS-1 W	60	104±3	111	81	82	131	Na-HCO_3-Cl
7	Ashton WS	41	146±5	143	117	115	139	Na-HCO_3
8	Barrons HS	73	102±6	128	100	99	127	Na-HCO_3
9	Buhl-Wendell W	26	118±10	126	99	98	166	Na-HCO_3
10	INEL-1 W 2000	34	120±2	111	81	82	97	Na-HCO_3
11	Magic HS Landing W	72	107±3	140	114	112	151	Na-HCO_3
12	Ruby Farm W	39	129±14	110	80	81	56	Na-HCO_3
13	Shannon W	47	103±3	132	105	104	131	Na-HCO_3
14	Sturm W	NA	121±4	105	75	76	107	Na-HCO_3
15	Wayne Larson W	22	120±16	134	107	105	107	Na-HCO_3
16	Cedar Hill W	38	123±5	116	87	87	143	Ca-HCO_3
17	Condie HS	52	78±9	97	67	68	117	Ca-HCO_3
18	N. Balanced Rock W	30	108±7	129	101	101	124	Ca-HCO_3
19	Robert Brown-2 W	25	78±8	93	62	64	95[e]	Ca-HCO_3
20	Warm WS	29	66±15	57	25	29	43	Ca-HCO_3
21	Green Canyon HS	44	68±8	72	40	43	73	Ca-SO_4
22	Liddy HS	50	113±5	85	54	56	102	Ca-SO_4
23	Yandell WS	32	55±20	67	35	39	70	Ca-SO_4

a. W = well, WS = warm spring, HS = hot spring
b. One standard deviation
c. No steam loss
d. Mg-corrected, as suggested by Fournier and Potter (1979)

4.11 Fluid Chemistry (pH, Salinity, Total Dissolved Solids, Etc.)

ESRP volcanic rocks have distinct rhyolitic and basaltic compositions. The rhyolitic rocks are older and lie beneath the thick sequences of younger basaltic flows. Rhyolitic rocks are alkali- and silica-rich rocks whereas basaltic rocks are alkali- and silica-poor rocks. Greater than 95% of the solute budget in the aquifer is composed of eight ions: calcium, magnesium, sodium, potassium, silica, bicarbonate, chloride, and sulfate. Commonly occurring phases that are undersaturated in the aquifer are plagioclase, pyroxene, intersertal mafic and silicic glass, and olivine. The pH in the aquifer ranges from 7.6 to 8.6 and increases with residence time. Groundwater chemistry changes with residence time along the direction of flow and with depth; the most notable changes are increases in Na, K, SiO_2, and Cl^- and decreases in $Ca^{2}+$, $Mg^{2}+$, HCO_3^-, and SO_{42}^-.

Typical ESRP thermal water (Table 3) is low TDSs Na-K-HCO_3 type water indicative of equilibration with the rhyolitic rocks hosting the deep geothermal system. However, there is a range of thermal water chemistry from Na-K-HCO_3 to Ca-Mg-HCO_3 water depending on the degree of equilibration with the source rock and or mixing with Ca-Mg-HCO_3 waters from the upper portion of the aquifer. Speciation calculations for water from the deep thermal system indicate that the deep system is supersaturated with respect to chalcedony/quartz, calcite, smectites clays, and zeolites. The apparent supersaturation of calcite in these deep thermal waters may reflect the fact that sampled water may have lost CO_2 prior to sampling. Similarly, speciation calculation shows that chalcedony and quartz are slightly oversaturated in these waters. Diagenetic calcite is common in the upper productive portion of the aquifer but diminishes with depth and is replaced by the aforementioned smectite clays and zeolites.

Table 3. Data from surface water, shallow wells, and deep well in and near the INL Site.

Location	Type of Sample	Ca mg/l	Mg mg/l	K mg/l	Na mg/l	SO_4 mg/l	Cl mg/l	HCO_3 mg/l	$^{87/86}Sr$ --
Condie Hot Springs	Hot spring	61.3	11.5	18	58.1	26.6	13.6	361.5	0.71440
Liddy Hot Springs	Hot spring	88	16	15	27	200	6.7	174	0.71082
Warm Spring	Warm spring	60.2	23.1	3.66	11.1	175	8.9	158.6	0.71434
Sturm	Deep well	3.8	.02	.84	32.1	4.56	3.0	74	0.70871
INEL-1, >1,460 m (Anion data from Mann [1986])	Deep well	7.0	.5	7.3	385	99	12	740	0.70980
INEL-1, 1,066–1,460 m (Anion data from Mann [1986])	Deep well	8.9	1.1	8.1	370	97	13	670	Not analyzed
INEL-1, 140–204 m (Anion data from Mann [1986])	Deep well	8.2	2.0	10	92	32	17	210	0.70935
Big Lost River	Surface water	37.5	9.9	1.4	5.8	18	4.8	200	0.71056
Little Lost River	Surface water	31.1	12.6	1.2	6.5	16	8.8	177	0.71256
Birch Creek	Surface water	41.2	14.3	1.5	6.1	4.5	25	164	0.71198
Yellowstone Plateau	Ground-water	10.1	6.2	9.06	4.5	3.5	3.7	63	0.70930
Site 17	Ground-water	54	17	1.3	10	16	11	228	0.710912

Vertical temperature profiles, the distribution of hydrothermal alteration and mineralization, and groundwater chemistry in the aquifer indicate that the ESRP aquifer is composed of two parts: an upper, cold, fast-moving aquifer and a deep, slow-moving geothermal system. The shallow (or productive) portion of the aquifer occurs from the water table (60−>200 m [197−>656 ft] below land surface), to a depth of 300 to 500 m (984 to 1,640 ft) below land surface. Fast-moving (1.52−10.51 m [5–34.5 ft] per day), cold (9−15°C [48–59°F]), calcium- and magnesium-rich waters characterize this part of the aquifer

(Wood and Low, 1986). The deeper portion of the aquifer is characterized by slower moving (0.006−0.091 m [0.019–0.3 ft] per day), warm (>30°C [86°F]) water and has a higher Na-K ratio (Mann, 1986; McLing et al., 2002). Although a sharp contact between these two systems is not always observed, changes in geothermal gradients can be used to delineate the two systems.

Temperature profiles in deep wells (Figure 5) show a break in slope from an upper isothermal gradient (nearly constant temperature with depth) to a deeper, moderately steep conductive gradient (rapid temperature rise with depth). This break in slope is interpreted as the effective base of the upper productive aquifer and the top of the deep geothermal system. Drill core collected from some of the deep wells show that this break in slope also corresponds to the inception of hydrothermal alteration and secondary mineralization of basalts beneath the upper aquifer (Neupane et al., 2014). The occurrence of mineral alteration is important, because it results in the sealing of conductive structure within the aquifer, causing permeability to dramatically decrease and allowing high heat flow from below to dominate aquifer temperature below this horizon. Using these breaks in slope as a guide, aquifer thickness in the study area ranges from near 0 near the proposed FORGE study site to about 400 m (1,312 ft) in the center of the plain. Deep channels of cold aquifer water characterize the thickest portions of the aquifer with very sharp inflection to the regional thermal gradient at depth.

Groundwater temperatures and borehole temperature profiles provide unique insight into the geometry of the ESRP aquifer and generally support the conclusions of the isotope-preferred flow path studies (Morse and McCurry, 2002; Johnson et al., 2000; Roback et al., 2001). For example, groundwater temperature at the top of the aquifer beneath the INL Site ranges from less than 8°C (46°F) to more than 18°C (64°F). The coldest of this water correlates with the preferential flow corridors identified by Roback et al. (2001) and is associated with areas where cold recharge moves rapidly through the system. In contrast, regions where water temperature is warmer generally correlate with the slower flow regions identified by the previous studies, providing support for the conclusion that in areas where water temperature is higher, groundwater flow is slow enough that high heat flow from below strongly influences water temperature or that exceptionally vigorous upwelling of geothermal water penetrates upward into the shallow aquifer. The conclusions presented in this paper represent the results of a three-dimensional synthesis of existing aquifer temperature data and examine the use of temperature distribution in the ESRP aquifer to constrain aquifer geometry, groundwater flow directions, and locations of potential shallow geothermal EGS resources.

4.11.1 Scaling Potential

The chemistries of the shallow ESRP aquifer and INEL-1 water are provided in Table 3. Water in the ESRP aquifer, which would be the working fluid in an EGS in the GRRA, is generally of very high quality, with TDS ranging from 170 to 2,200 mg/L (although TDS >500 ppm is rare). This indicates a potential for scaling not significantly different than that of a hydrothermal resource at similar temperatures. As such, approaches used in hydrothermal systems to minimize scaling should be applicable to operation at the GRRA.

Silica levels in ESRP aquifer water are low, but at elevated temperature, the silica would approach the solubility of quartz or chalcedony shortly after circulation through the reservoir begins. Formation of silica in the surface equipment can be minimized by controlling the amount of heat extracted from the produced fluid to ensure that the injected fluid is at a temperature above the solubility of amorphous silica. Once the injected fluid is returned to the reservoir, the potential for the precipitation of silica as quartz or chalcedony will diminish as the fluid is reheated.

Unlike silica, the solubility of carbonate varies inversely with temperature. Because the carbonate level in the shallow aquifer is relatively high, there is potential for carbonate precipitation when the fluid is heated and the carbonate solubility decreases. The precipitation of carbonate as calcite will occur as the partial pressure of the CO_2 exceeds the fluid's excess pressure above saturation. This is avoided with typical hydrothermal fluids by the use of pumping to maintain an excess pressure greater than the partial pressure of the dissolved CO_2. It is anticipated that a similar approach can be used at the GRRA.

4.11.2 Corrosion Potential

The chemistries of the typical shallow ESRP aquifer and INEL-1 water shown in Table 3 with low TDS, circum neutral pH, and the low chloride concentration suggest low corrosion potential for infrastructure associated with an EGS operation. Corrosion potential, of course, increases as the fluid is heated and different rock constituents dissolve during circulation; however, it is not expected that the potential will be appreciably greater than that of a similar temperature hydrothermal resource. During operations, corrosion potential will be minimized by reducing the potential for scaling (and associated galvanic corrosion and pitting) and by selection of compatible materials for component surfaces exposed to the EGS fluids. Unless information characterizing the reservoir indicates a probability of an unexpected change in fluid chemistry (such as pH), it is probable that carbon steel will suffice as the primary material of construction for equipment and piping systems. Exceptions to this may include the materials used for thin-walled heat exchanger surfaces (tubes), where it may be necessary to use a more compatible material in order to allow for extended testing (multiple years).

4.11.3 Ability to do Chemical Stimulations

The deep thermal reservoir of the GRRA is anticipated to consist of rhyolite with abundant plagioclase and clinopyroxene and secondary zeolites, clays, and calcite. The stability of these minerals and their resistance to chemical alteration combined with the overall lack of connected permeability makes it unlikely that the EGS target zone would be amenable to chemical stimulation.

4.11.4 Reservoir Short-Circuiting due to Potential Precipitation (or Dissolution)

It is expected that the injection of Ca-HCO_3-type ESRP aquifer water into the deep Na-K-HCO_3 water that is in the proposed EGS zone could cause the introduced water to precipitate carbonate during equilibration. However, the amount of calcite that could be precipitated in the EGS zone is small relative to the total reservoir size. In general, the mixing of injected groundwater with the preexisting (if any) EGS water could create a chemical environment for enhanced leaching/dissolution. However, the residence time for the likely flow-back water after hydraulic fracturing is expected to be much shorter (days to weeks) than the many thousand years (ca. 35 kyr) of residence time of the deep thermal water (Mann, 1986).

4.12 Mechanical Behavior of Reservoir

Mechanical behavior of the reservoir rocks likely to be encountered in the GRRA can be estimated from drilling behavior in wells intersecting the rhyolite rocks in the ESRP or from analysis of specimens of the rhyolite. Few borehole breakouts indicating borehole deformation were encountered in INEL-1, and, without knowledge of the strength of the rocks at the breakout depths, stress estimates from them are ambiguous (Wood et al., 2007). Therefore, to provide preliminary data on the material behavior of rocks that will be encountered in geothermal explorations in the GRRA, two specimens from INL Well W-02 were tested at the University of Oklahoma's Mewbourne School of Petroleum and Geological Engineering Laboratory. Indirect tensile strength was measured using Brazil test methods (ISRM, 1978) (Figure 22). These tests were performed using a servo-hydraulic rock mechanics testing system (MTS 810), and the specimens were loaded using force control until failure. The indirect tensile strength of the specimens was calculated from

$$\sigma_t = \frac{2P}{\pi Dt} \quad (1)$$

where σt is the Brazilian tensile strength (MPa); P is the load at failure (N); D is the diameter of the specimen (mm); and t is the thickness of the specimen (mm). Indirect tensile strength of the specimens ranges from 2 to 3 MPa (290 to 435 psi) with an average value of 2.56 MPa (371.30 psi). For our purposes, we assume that the tensile stress (σ_T) is 3.44 MPa (500 psi).

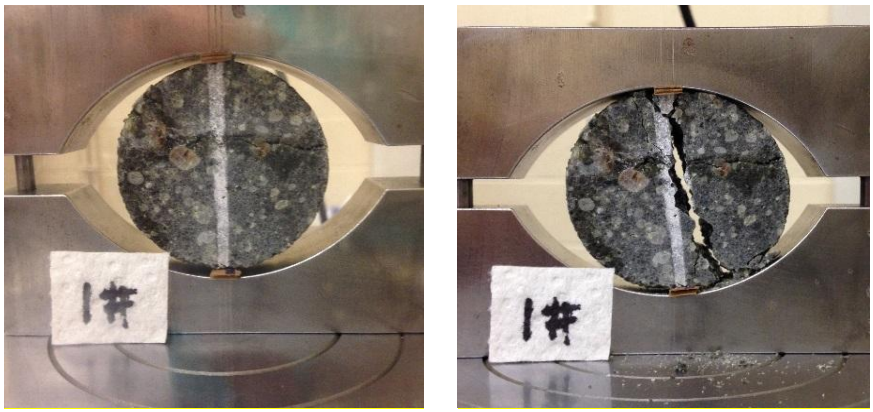

Figure 22. Brazilian testing of a core sample taken from INL Well W-02 before and after testing.

An approximate wellbore pressure needed to fracture the rhyolite can be estimated using elasticity theory if the minimum and maximum stress states in relation to the wellbore are known and the tensile failure of the rock is also known. For this analysis, we will assume the well is horizontal at a depth of 3.5 km (~11,500 ft) and aligned with the minimum stress state. We further assume that the maximum stress state is the lithostatic load and can be estimated using the depth of interest multiplied by 0.025 MPa/m (1.1 psi/ft) (i.e., σ_max= 87.2 MPa [12,650 psi]) and the minimum stress perpendicular to the wellbore is half the maximum stress (i.e., σ_min= 43.6 MPa [6,325 psi]). Elastic theory would predict the breakdown pressure (pb) as:

$$p_b = 3\sigma_{\min} - \sigma_{\max} + \sigma_T \quad (2)$$

where σ_min is the minimum stress, σ_maxis the maximum stress, and σ_T is the tensile failure strength. For this case, the breakdown pressure is 47.1 MPa (6,825 psi). The hydraulic head of a standing column of water within this wellbore is 34.5 MPa (5,000 psi) and suggests that approximately 13.8 MPa (2,000 psi) of wellhead pressure would be needed to induce fracturing. Although the actual in situ stress states are not known at this time, this preliminary analysis suggests that conditions are generally favorable for creation of fractures in the deep rhyolites at the INL Site.

4.13 Wellbore Stability and Hydraulic Fracture Design

Knowledge of the in situ stresses allows optimization of drilling mud weights, the design of stable wellbore trajectories, assessment of the stability of uncased wells, and the evaluation of casing schemes. For example, based on the geomechanical model, it is straightforward to calculate the safe mud window for drilling wells for any well trajectory (Figure 23).

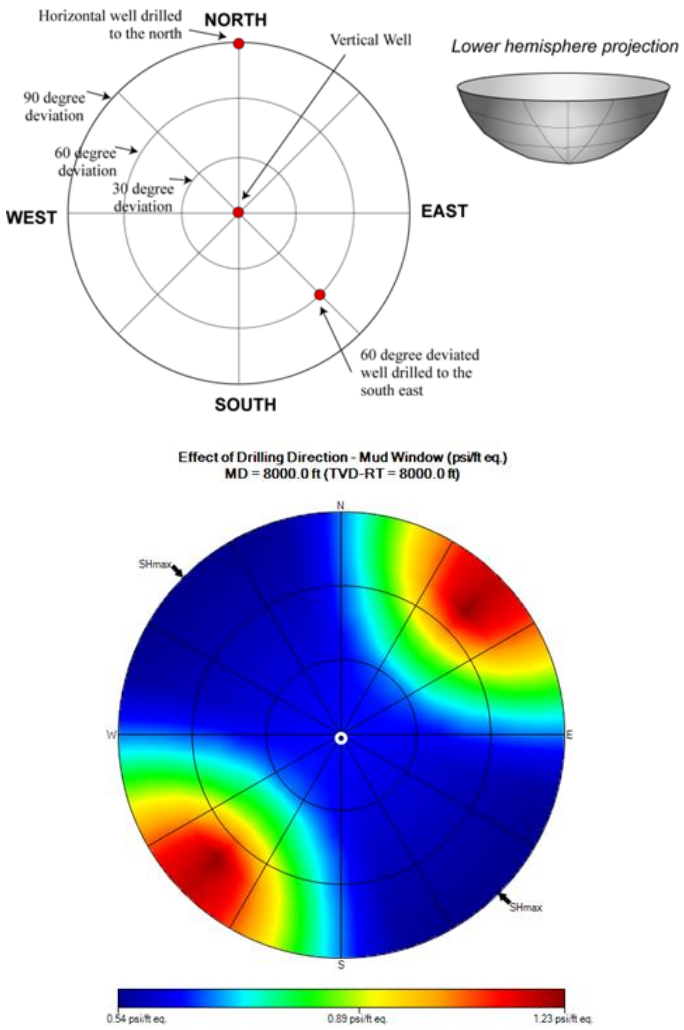

Figure 23. Diagrammatic sketch indicating all possible well trajectories in the lower hemisphere projection (upper) and the safe mud weight window for drilling based on the geomechanical model.

Of equal importance to drilling is the application of the geomechanical model to well completion design, specifically the ability to hydraulically fracture the rock at the desired depth in the reservoir. With the geomechanical model, the optimal trajectory to initiate hydraulic fractures and for these fractures to link up and grow away from the wellbore can be determined (Figure 24).

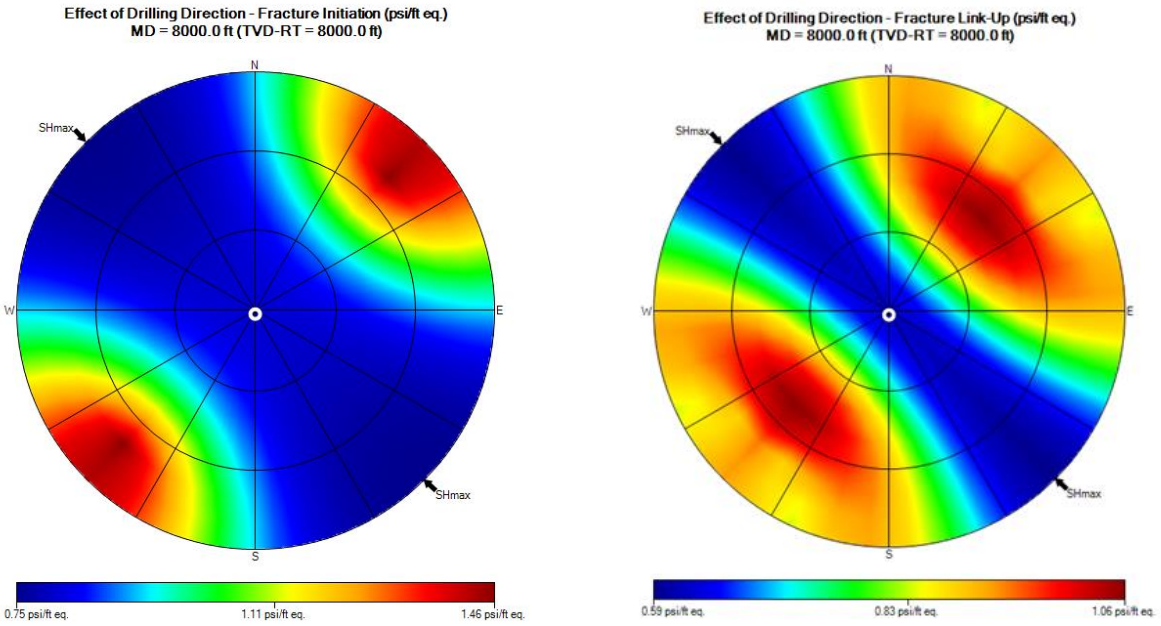

Figure 24. Optimal trajectories to initiate (left) and link up (right) hydraulic fractures based on the geomechanical model.

4.14 Geologic Mapping

Numerous studies have developed surficial geologic maps of the ESRP, and many of these focus on the volcanic features of the region. Kuntz et al. (1994) produced a geologic map of the INL area and an excerpt from that map, roughly centered on the GRRA (Figure 25), illustrates how the GRRA is situated at the foot of mountain ranges composed of sedimentary rocks within the basaltic lava flows of the ESRP.

The geology of the subsurface is inferred from boreholes, geophysics, and regional structural interpretations. Ackerman et al. (2006) summarizes such sources in a regional cross-section that runs from the southwest to the northeast of the ESRP (Figure 26), illustrating the relative relationship of basaltic and rhyolitic volcanics on the edges of the plain.

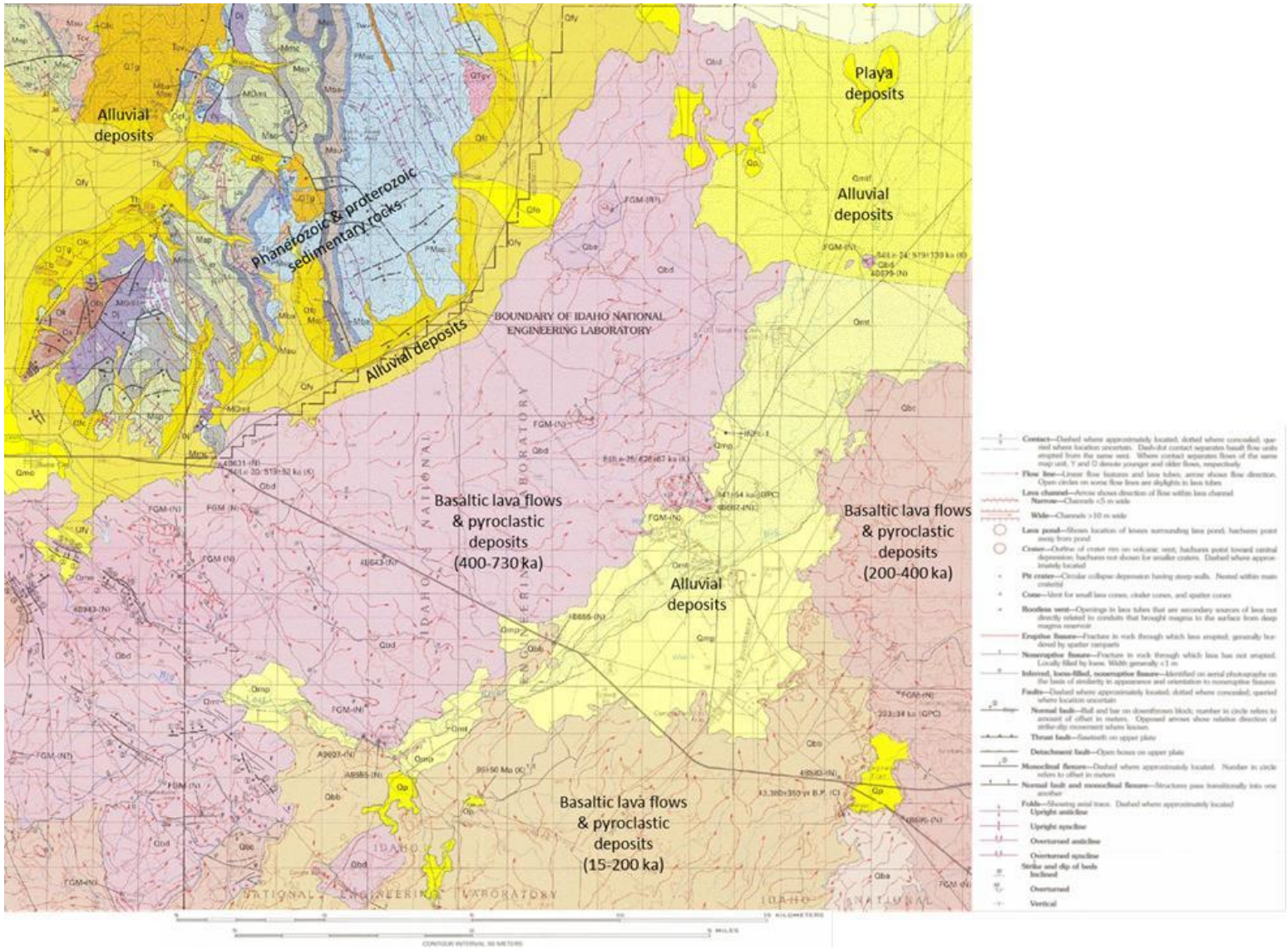

Figure 25. Excerpt from the "Geologic map of the Idaho National Engineering Laboratory and adjoining areas, eastern Idaho," by Kuntz et al. (1994) showing primary surficial geologic features in the region surrounding the GRRA.

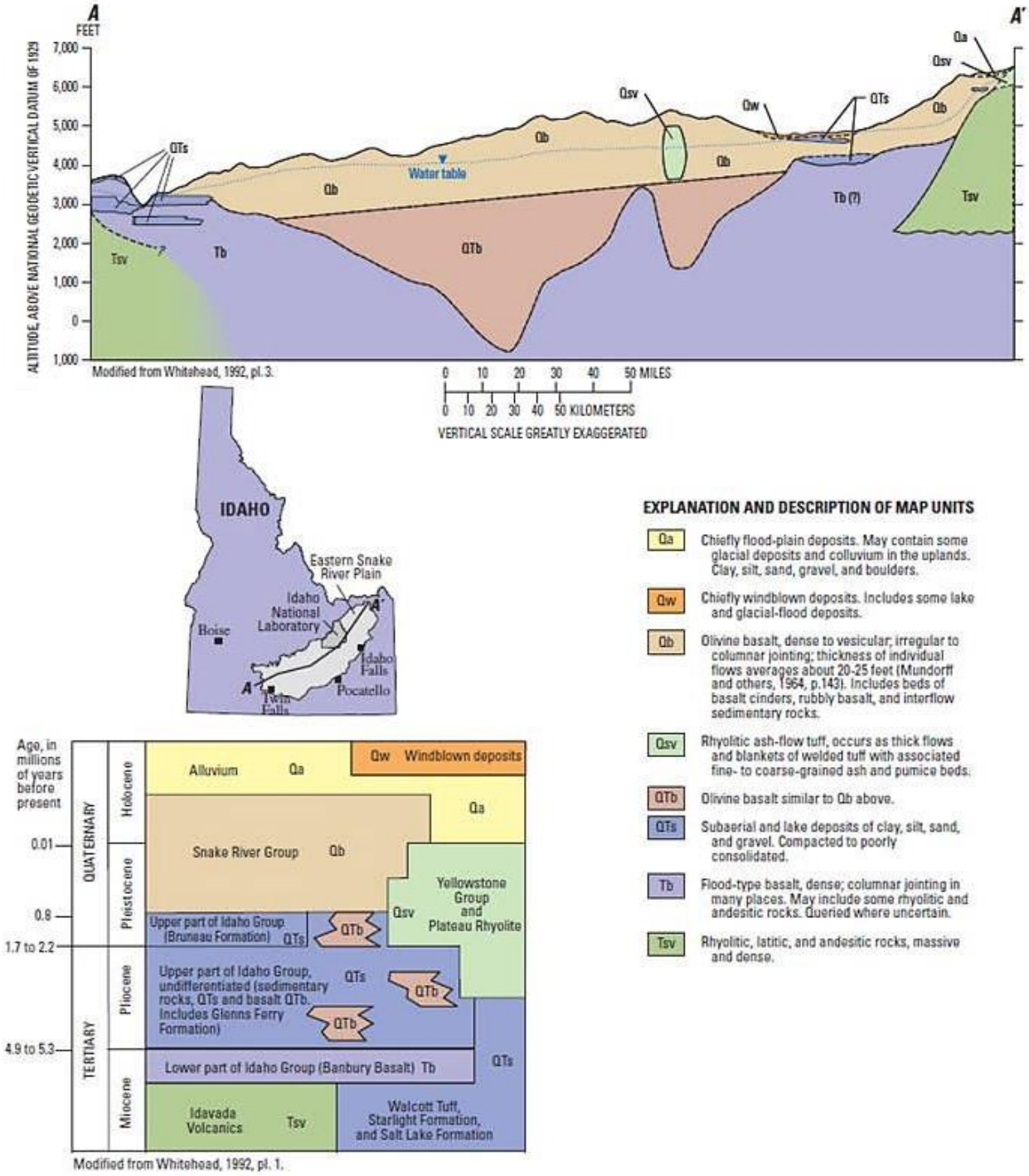

Figure 26. Generalized geology, water table altitude, and geologic groups and formations, as well as generalized stratigraphy of the ESRP, Idaho (Akerman et al., 2006).

4.15 Conceptual Model

The subsurface of the ESRP consists of thick rhyolitic ash-flow tuffs, which are overlain by >1 km (0.6 mi) of Quaternary basaltic flows. The rhyolitic volcanic rocks at depth are the product of super-volcanic eruptions associated with the Yellowstone Hotspot. These rocks progressively become younger to the northeast toward the Yellowstone Plateau (Hughes et al., 1999; Pierce and Morgan, 1992). The younger basalt layers are the result of many low-volume, monogenetic, shield-forming eruptions of short duration that emanated from northwest-trending volcanic rifts in the wake of the Yellowstone Hotspot (Hughes et al., 1999). A thermal anomaly extends deep into the mantle beneath the ESRP, and the province has some of the highest calculated geothermal gradients (Figure 1) in North America. This gives the ESRP potential to be one of the highest producing geothermal districts in the United States. The thick sequences of coalescing basalt flows with interlayered fluvial and eolian sediments in the ESRP constitute a very productive aquifer system above the rhyolitic ash-flow tuffs (Shervais et al., 2013; Whitehead, 1992; Nielson et al., 2012). Elevated heat flow is typically highest on the margins of the ESRP and lowest along the axis (center) of the plain, where thermal gradients are suppressed by the ESRP aquifer. Beneath the aquifer, however, thermal gradients rise again and may tap even higher heat flows associated with the intrusion of mafic magmas into a geophysically imaged mid-crustal sill complex (Shervais et al., 2011). High thermal fluxes in the ESRP were first documented in the early 1970s (Brott et al., 1976). Heat flow values in excess of 110 mW/m^2 have been calculated below the ESRP aquifer; values over 150 mW/m^2 have been projected for depths to 6 km (19,685 ft) (Blackwell and Richards, 2004).

Recent volcanic activity, a high heat flux, and the occurrence of numerous peripheral hot springs suggest the presence of undiscovered geothermal resources in the ESRP (McLing et al., 2016; Nielson and Shervais, 2014). These geologic indicators suggest that the ESRP at depth hosts a large geothermal resource with the potential for one or more viable conventional or enhanced geothermal reservoirs. In particular, the lower welded rhyolite ash-flow tuff zone may have exploitable heat sources that can be tapped by EGS development. However, masking of the geothermal systems is a huge volume of cold groundwater moving through the ESRP aquifer (McLing et al., 2016; Morse and McCurry, 2002), which originates as snowmelt from the Yellowstone Plateau and surrounding mountain basins through the overlying prolific ESRP aquifer.

5. SURFACE DATA

5.1 Thermal Characteristics

5.1.1 Average Ground Surface Temperature

The ground surface temperature across the ESRP is generally ranges from 10 to 15°C (50 to 59°F), as measured in numerous vadose zone temperature profiles and in multi-year monitoring of surface temperature at the INL Site (Akerman et al., 2006).

5.1.2 Surface Heat Flow

The upward heat flux on the ESRP above the regional aquifer has been calculated to be ~27 mW/m^{-2} (Pittman, 1994).

5.1.3 Regional Heat Flow

Heat flow below the aquifer is ~110 mW/m^2 (137% of the average in the Basin and Range Province). A map developed by SMU of heat flow in the United States illustrates the relatively high heat fluxes in the ESRP and is included as Figure 5.

5.2 Gravity Data

Regional and detailed gravity surveys have been conducted in the ESRP and adjacent Basin and Range. Early regional gravity studies were conducted to assess the compositions of the ESRP crust relative to the surrounding Basin and Range crust (Smith et al., 1996). Additional detailed gravity studies were performed to assess possible boundary faults near the southernmost ends of the Lost River and Lemhi ranges. More recent compilations of gravity data and processing have produced Bouguer, isostatic residual, vertical derivative, intermediate-wavelength, long-wavelength, and maximum horizontal-gradient maps of the ESRP (Mabey, 1982). These data, along with aeromagnetic data, have been used to delineate deep-seated crustal structures to assess controls on regional fluid flow (Mankinen et al., 2004). The gravity and aeromagnetic data for the ESRP are available at the Pan American Center for Earth and Environmental Studies at the University of Texas at El Paso.

5.3 Chemistry

The ESRP aquifer lies above hot volcanic rock and is one of the largest and most productive aquifers in the United States. Recharge to the aquifer primarily comes from snowfall in the highlands bordering the plain and from infiltration of water from irrigation, canals, rivers, and reservoirs. Groundwater flows southwesterly beneath the plain and is discharged to the Snake River in the Thousand Springs Area near Hagerman, Idaho, approximately 209 km (130 mi) southwest of the INL Site. Water in the aquifer is cold (<13°C [<55°F]), primarily contained in highly permeable basalt flows, and generally characterized as Ca-Mg-CO_3 water, which is typical of western aquifers (see Table 3). Water samples from deep ESRP wells (Sturm well and INEL-1, Table 4) indicate that the existing water in the deep formations is good-quality, Na-HCO_3 type water having low TDS and low concentrations of major and trace elements.

Table 4. Typical chemical concentrations in water samples for the ESRP shallow-aquifer, deep-thermal system.

Constituents	Shallow ESRP Aquifer Water (mg/L)	INEL-1Water (mg/L)
pH	7.8	8.2
Ca	43	8.1
K	3	8.3
Mg	16	0.9
Na	14	363
SiO_2(aq)	24	40
Fe	0.06	1.0
Mn	0.005	0.07
Li	0.008	0.29
Al	0.005	—
As	0.002	0.03
Sr	0.2	0.14
Ba	0.06	—
B	0.03	0.56
HCO_3	180	830
F	0.3	12.7
Cl	25	14
SO_4	24	88
TDS	450	964

5.4 Aerial Photography

INL has an extensive aerial photography library dating back to 1993. The photographs are used for high-resolution mapping, GIS data layer development, and tracking change over time. Resolution levels of this library vary from 0.1-m (4-in.) pixels on and around all facility areas to 1.5-m (5-ft) pixels for the INL Site proper and surrounding areas. The oldest imagery from 1993 is black and white, while all imagery captured after 2000 is full color (red, green, blue) and near infrared for imagery captured after 2011.

5.5 Remote Sensing

Satellite imagery has been collected for INL and surrounding areas for various years over the past 3 decades. This imagery includes LandSat MSS, LandSat Thematic Mapper, MODIS, QuickBird, and GeoEye. Spectral and spatial resolutions vary across these different platforms. Remote-sensing and image-processing products derived from these data include fire-boundary mapping, vegetation-classification layers, change-detection maps, and snow-cover estimate mapping.

6. GEOLOGIC CONDITIONS

Information contained in the following subsections supports the evaluation of the structure and stress regime and the microseismic survey.

6.1 Regional Stress Direction and Strain Rates

Compilations of minimum, principal stress directions show the state of stress in the Basin and Range Province northwest of the ESRP is characterized by northeast-southwest extension, as indicated by focal mechanisms that include those for the Borah Peak mainshock and aftershocks (Doser and Smith, 1985; Eddington et al., 1987; Richins et al., 1987; Smith et al., 2009) and by a fault orientation analysis performed by Stickney and Bartholomew (1987). Horizontal Global Positioning System (GPS) velocity results reveal a northeast-southwest extensional strain rate consistent with the northwest-trending normal faults and focal mechanisms (Payne et al., 2012).

Within the ESRP, a northeast-southwest-oriented extensional stress is inferred from the orientation of fissures within the Holocene rift zones (Pierce and Morgan, 1992; Zoback and Zoback, 1989). GPS-derived strain rates for the SRP suggest a very low rate of deformation (Payne et al., 2012). Smaller gravitational potential energy variations within the SRP due to flat topography and a denser crustal composition may in part explain the lower rate of deformation (Payne et al., 2008). The lack of borehole breakouts in INEL-1 (Moos and Barton, 1990) are consistent with this regime.

GPS data suggest that rapid extension in the Basin and Range Province in the Centennial Tectonic Belt adjacent to the much more slowly deforming region of the SRP results in right-lateral shear within a narrow zone between them. Within the Centennial Shear Zone, components of deformation may be due to regional-scale rotation, strike-slip faulting, and distributed simple shear or some combination of these (Payne et al., 2012). The GRRA is located adjacent to the Centennial Shear Zone. The GRRA is also along the SRP physiographic boundary where possible northeast-trending normal faults are identified in the subsurface (Pankratz and Ackermann, 1982; Sparlin et al., 1982; Stanley, 1982), which could accommodate right-lateral strike-slip motion.

6.2 Seismic Array in Place and Data

Since 1972, INL has supported a seismic monitoring program and has monitored earthquake activity on and near the SRP. The INL Seismic Monitoring Program provides earthquake data and staff to support nuclear operations through continuous monitoring of earthquake activity. Staff also develop seismic design criteria and perform assessments of seismic and volcanic hazards for existing and new facilities.

The INL Seismic Monitoring Program currently operates 32 permanent seismic stations to determine the time, location, and size of earthquakes occurring in the vicinity of the INL Site (Carpenter et al., 2011). Seismic stations are located within and around INL near potential earthquake sources that include major range-bounding normal faults and volcanic rift zones. The seismic network within INL Site boundaries has an average station spacing of 20 km (12 mi) and a detection threshold of approximately Magnitude 0.1. There are seven seismic stations that surround and are located within 10 km (6 mi) of the proposed FORGE site. GPS receivers are collocated at 16 seismic stations to determine rates of crustal deformation and locations of active seismic regions. Three GPS receivers are located at seismic stations that are within 10 km (6 mi) of the GRRA. Figure 27 shows the location of seismic stations used by the INL Seismic Monitoring Program.

The INL Seismic Monitoring program also operates 31 accelerometer sites for the purpose of recording strong ground motions from local, moderate, or major earthquakes. Eight of the accelerometers are located within INL buildings to determine the response of these buildings to ground motions in the event of a large earthquake. The others are located at "free-field" sites (not within buildings) at INL facility areas and seismic stations. The free-field data are used to determine the levels of earthquake ground motions at the ground (rock or soil) surface and to assess crustal attenuation of small- to large-magnitude normal faulting earthquakes.

The INL seismic network has been operational for decades, and its associated data are a benefit to establishing and operating FORGE. These provide a verifiable baseline that is unparalleled and documents quiet seismic conditions, which will provide an excellent framework to assess FORGE activities.

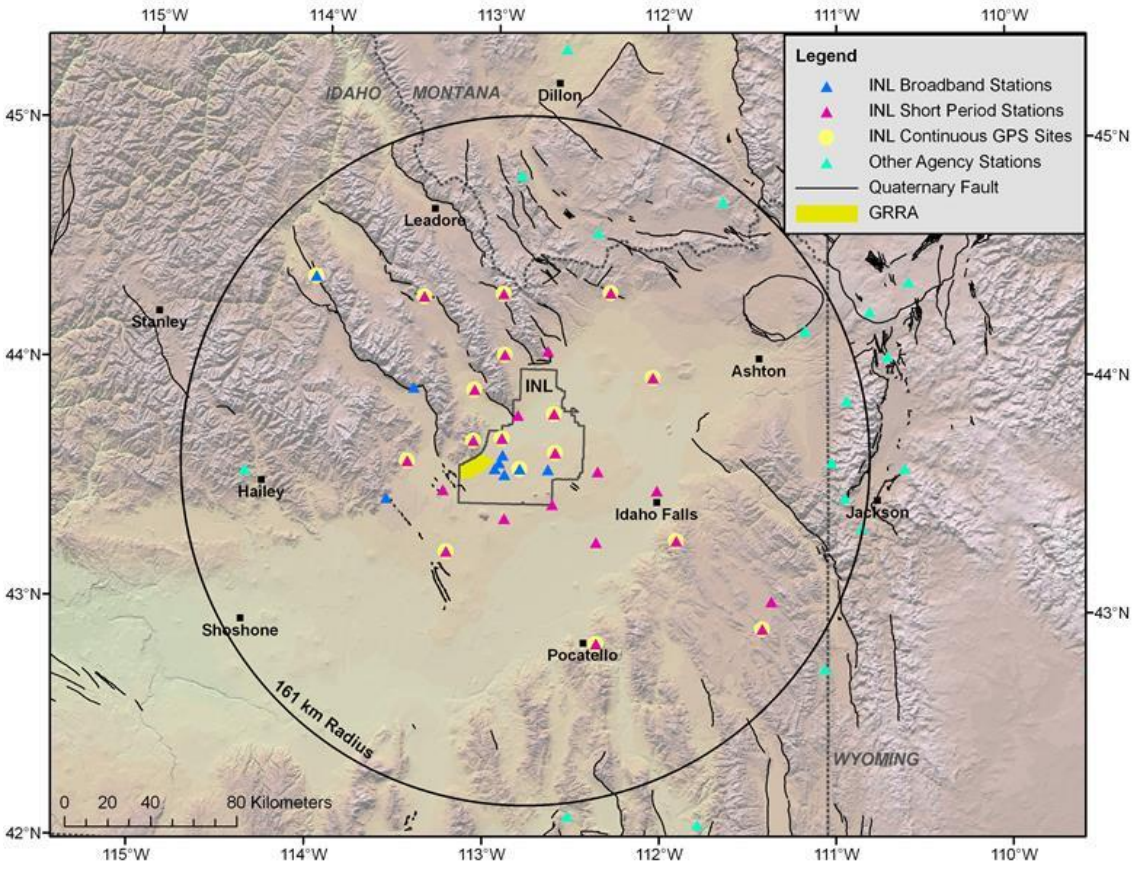

Figure 27. Locations of INL seismic stations and stations monitored by INL that are operated by other institutions (Carpenter et al., 2011).

6.3 Orientation and State of Stress

Compilations of minimum, principal stress directions show the state of stress in the Basin and Range Province northwest of the SRP is characterized by northeast-southwest extension, as indicated by focal mechanisms, including those for the Borah Peak mainshock and aftershocks (Doser and Smith, 1985; Eddington et al., 1987; Richins et al., 1987; Smith et al., 2009) and by a fault orientation analysis performed by Stickney and Bartholomew (1987). Horizontal GPS velocity results reveal a northeast-southwest extensional strain rate consistent with the northwest-trending normal faults and focal mechanisms (Payne et al., 2012) (Figure 28).

Within the SRP, a northeast-southwest-oriented extensional stress is inferred from the orientation of fissures within the Holocene rift zones (Pierce and Morgan, 1992; Zoback and Zoback, 1989). GPS-derived strain rates for the SRP suggest a very low rate of deformation (Payne et al., 2012). Smaller gravitational potential energy variations within the SRP due to flat topography and a denser crustal composition may, in part, explain the lower rate of deformation (Payne et al., 2008). The lack of borehole breakouts in INEL-1 (Moos and Barton, 1990) are consistent with this regime.

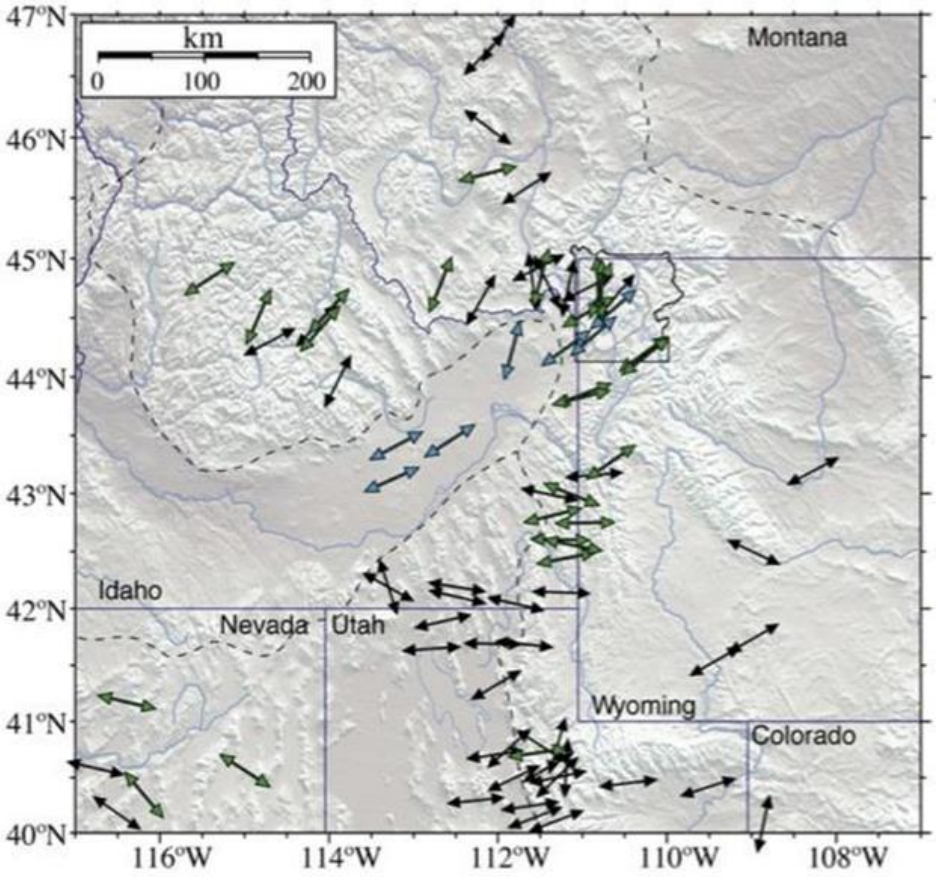

Figure 28. Stress field of ESRP and surrounding Basin and Range illustrating dominant lithospheric northeast-southwest extension (Eddington et al., 1987; Blackwell et al., 1992).

GPS data suggest that rapid extension in the Basin and Range Province in the Centennial Tectonic Belt adjacent to the much more slowly deforming region of the SRP results in right-lateral shear within a narrow zone between them. Within the Centennial Shear Zone, components of deformation may be due to regional-scale rotation, strike-slip faulting, and distributed simple shear or some combination of these (Payne et al., 2012). The GRRA is located adjacent to the Centennial Shear Zone. The GRRA is also along the SRP physiographic boundary, where possible northeast-trending normal faults are identified in the subsurface (Pankratz and Ackermann, 1982; Sparlin et al., 1982; Stanley, 1982), which could accommodate right-lateral strike-slip motion.

Taken as a whole, the preliminary analysis of the stress regime is favorable for creating and maintaining an EGS reservoir. The inferred maximum principal stress direction is downward, and northeast-southwest-oriented extension creates an environment where high-angle (vertical) fractures are preferred and the extensional stresses would act to keep created fractures open.

6.3.1 Probabilistic Seismic Hazard Analysis

INL completed computations for a probabilistic seismic hazard analysis (PSHA) in 2000 (Waite and Smith, 2004;Woodward-Clyde Federal Services et al., 1996). The PSHA estimated ground-motion levels at return periods of 2,500 and 10,000 years for earthquake sources and ground-motion models specific to the SRP and Basin and Range Province. The seismic source characterization models included fault-specific sources, background seismicity within the Basin and Range Province, volcanic rift zone earthquake sources, and a random earthquake source within the SRP. Each of the source models is characterized by the geographic locations, magnitude distributions, and recurrence models. Results of the PSHA indicate that hazard is driven by the fault-specific sources, which are capable of Moment-Magnitude 7+ events and background seismicity of the Basin and Range (Moment Magnitude <6.5). The hazard results also showed that for return periods shorter than 10,000 years, volcanic earthquake source zones do not contribute significantly to hazard levels, because their recurrence estimates are much longer (>16,000 years) and their maximum magnitudes are lower. The 2000 PSHA is the basis for seismic design levels, which are currently used for structural design of new, and safety qualifications of existing, INL facilities.

6.4 Paleo-Seismic Data

The southern ends of three prominent northwest-trending, southwest-dipping crustal normal faults are located along the western boundary of the INL Site. The GRRA is located between the southern ends of the Lost River and Lemhi normal faults. Paleoseismic data have been collected in eight trenches excavated across fault scarps along the two southernmost segments of the Lost River and Lemhi faults. The Arco segment of the Lost River fault is closest to the southern end of the GRRA. Two trenches excavated in Quaternary sediments show fault offsets as recent as 15,000 to 25,000 years ago on the Arco segment. The trench logs record repeated offsets by paleoearthquakes that are temporally clustered and extend back in time to ~160,000 years (Woodward-Clyde, 1992). The southernmost trench, which is located in the Arco Volcanic Rift Zone and within the projected trend of the Arco segment, showed no fault offsets but instead deposits consistent with a river terrace (Smith et al., 1996; Woodward-Clyde Federal Services et al. 1996; Payne et al., 2011). The South Creek segment of the Lemhi fault is closest to the northern end of the FORGE site. Two trench logs also show temporal clustering of paleoearthquakes, with the most recent events occurring 15,000 to 24,000 years ago (Wood et al., 2007; Olig et al., 1997; Olig, 1997).

6.5 Distance to Existing Faults, Type of Fault, and Size

The closest faults to the GRRA are the Lemhi and Lost River faults, which are prominent northwest-trending, southwest-dipping normal faults that are 150 km (93 mi) long and capable of Magnitude 7+ earthquakes. The most recent offsets along both faults occurred 15,000 to 25,000 years ago. The proposed location of the subsurface operations is 16 km (10 mi) south of the postulated subsurface rupture plane of the southernmost Lemhi fault segment (assuming a 50-degree southwest dip). The operational area of the GRRA is located 19 km (12 mi) north of the southernmost Lost River fault segment (Figure 27).

6.6 Level of Seismic Activity

Compilations of historical seismicity that include INL seismic monitoring catalogs indicate the SRP is relatively aseismic (Figure 29). The majority of earthquakes occur outside of the SRP in the surrounding Basin and Range Province (Eddington et al., 1987; Hemphill-Haley et al., 2000). From 1972 to 2011, the INL Seismic Monitoring Program has detected and located 70 microearthquakes of Local Magnitude <2.2 within the SRP; 16 of these have been located within the INL Site boundaries. Five of the 16 microearthquakes are located north of the GRRA, the largest of which is a Magnitude 2.2 (Payne et al., 2011). One of these microearthquakes (Coda Magnitude 0.9), which occurred in 1985, was located in the northern part of the INL Site (Hemphill-Haley et al., 2000). A 7-month-long microearthquake survey with 17 seismic stations spaced <2 km (<1.2 mi) apart was conducted in 1988 near the northern end of the GRRA (Jackson et al., 1989). Two microearthquakes (Magnitude <0.5) were detected by the temporary array and were located outside of the array and not in the GRRA.

Focal depths of earthquakes within the SRP near and within the INL Site are <11 km (<7 mi) and thought to be tectonic in origin. Twenty-five deep (>15 km [>9 mi]) microearthquakes have been located near the northern part of the Great Rift (50 km [31 mi] south of INL) and are interpreted to be related to fluid movement or of volcanic origin (Payne et al., 2011; Jackson et al., 1989).

Taken as a whole, the preliminary analysis of the stress regime is favorable for creating and maintaining an EGS reservoir. The inferred maximum principal stress direction is downward, and northeast-southwest-oriented extension creates an environment where high-angle (vertical) fractures are preferred and the extensional stresses would act to keep created fractures open.

7. EXISTING WELLS AND WELL DRILLING

Several observation and monitoring wells are located within and near the boundary of the GRRA. The USGS will core a groundwater-monitoring well near the site selected for FORGE during the summer of 2016. Additionally, the INEL-1 borehole is available for monitoring purposes but will require a fitness-for-use evaluation during Phase 2.

7.1 Depth of Existing Wells

Tables 5 and 6 list the total depth of wells on the INL Site. Table 5 shows the depth information for the well temperature data that have been collected. Table 6 lists the total depth of supplementary wells; temperature data currently is not available for the supplementary wells.

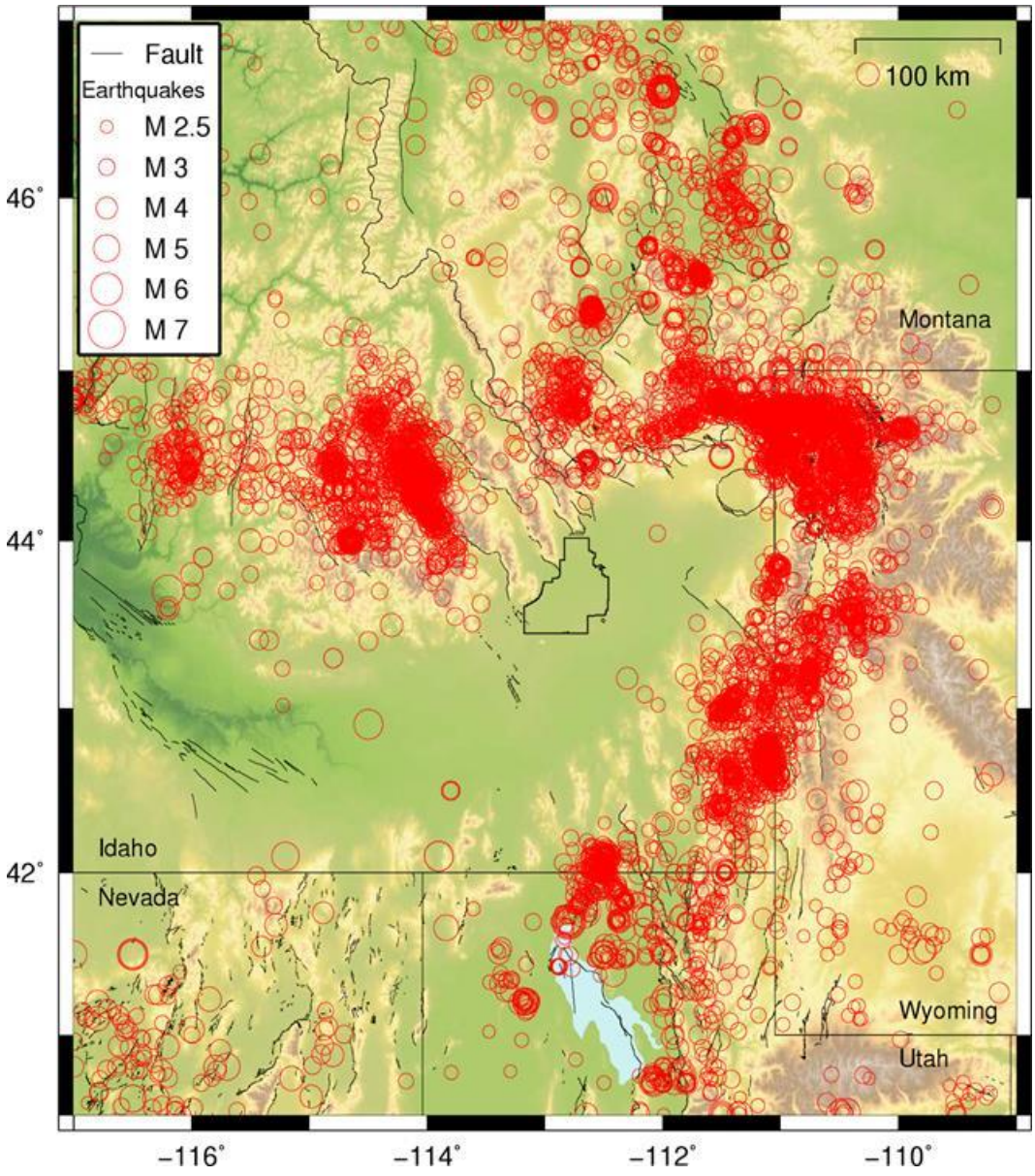

Figure 29. Distribution of earthquakes of magnitude greater than 2.5 in southeastern Idaho compiled from nearby regional seismic networks and the INL seismic monitoring network.

7.2 Well Type (Full-Sized, Corehole, Shallow-Gradient Holes)

For more than 50 years, INL in cooperation with the USGS has developed a resource of more than 150 monitoring wells of varying depths, diameters, and designs across the INL Site. These wells have been fully characterized, including borehole completion data, temperature profiles, geochemistry, gamma logs, etc. Additionally, more than 11,000 m (36,089 ft) of well core is available for study. Table 5 lists the nine deepest wells on the INL Site and their current status; in addition, Table 6 is a summary list of wells that are currently being monitored or have been used for significant studies in the recent past. The USGS will core a groundwater monitoring wells near the site selected for FORGE during the summer of 2016.

7.3 Well Status

Tables 5 and 6 show the status and purpose for regionally important wells at INL. These tables summarize only a fraction of the wells (more than 150 active wells) that exist and are available to support studies.

Table 5. Depth, type, and status of selected deep wells in the ESRP.

Well Name	Borehole Depth (m)	Well Type	Completion Zone	Status
INEL-1	3,159	Observation	Aquifer	Active
NPR-W-02	1,524	Corehole	Beneath aquifer	Uncertain
COREHOLE 2A	914	Observation	Aquifer	Active
COREHOLE 1	610	Observation	Aquifer	Active
ANL-OBS-A-001	582	Observation	Aquifer	Active
C1A	550	Corehole	Beneath aquifer	Uncertain

Table 6. Depth, type, and status of the supplementary wells on the INL Site.

Well Name	Borehole Depth (m)	Well Type	Completion Zone	Status
MIDDLE-1823	504	Monitoring	Aquifer	Active
USGS-015	456	Monitoring	Aquifer	Active
MIDDLE-2050A	435	Corehole	Aquifer	Active
USGS-105	429	Observation	Aquifer	Active
NRF-5	408	Observation	Aquifer	Active
ARA-3	408	Potable water/production	Aquifer	Inactive
USGS-137A	401	Monitoring	Aquifer	Active
USGS-103	398	Monitoring	Aquifer	Active
HIGHWAY 1(A),1(B),1(C)	397	Observation	Aquifer	Uncertain
TRA DISPOSAL	389	Observation	Aquifer	Active
USGS-131	378	Monitoring	Aquifer	Active
USGS-132	377	Corehole	Aquifer	Active
EOCR PRODUCTION WELL	377	Potable water/production	Aquifer	Inactive
USGS-108	371	Observation	Aquifer	Active
SPERT-2	371	Potable water/production	Aquifer	Active
USGS-013	366	Observation	Aquifer	Active
USGS-007	366	Observation	Aquifer	Active
USGS-131A	365	Monitoring	Aquifer	Active
USGS-135	365	Monitoring	Aquifer	Active
MIDDLE-2051	359	Corehole	Aquifer	Active
SITE-09	347	Observation	Aquifer	Active
QUAKING ASPEN BUTTE	340	Production	Aquifer	Active
TCH-2	339	Monitoring	Aquifer	Active

Table 6. (continued).

Well Name	Borehole Depth (m)	Well Type	Completion Zone	Status
WEAVER AND LOWE	328	Observation	Aquifer	Uncertain
EBR-1	328	Potable water	Aquifer	Active
FINGER'S BUTTE BLM	322	Domestic	Aquifer	Uncertain
SITE 01 WATER TABLE	321	Observation	Aquifer	Uncertain
USGS-136	319	Monitoring	Aquifer	Active
USGS-030A, 30B, 30C	307	Observation	Aquifer	Active
RWMC-MON-A-066	301	Monitoring	Aquifer	Active
TRA-04	296	Potable water/production	Aquifer	Active
USGS-134	289	Monitoring	Aquifer	Active
OMRE	287	Potable water/production	Aquifer	Active
NTP-AREA 2	267	Observation	Aquifer	Active
USGS-101	264	Observation	Aquifer	Active
SITE-19	264	Observation	Aquifer	Active
ARA-COR-A-005	262	Monitoring	Aquifer	Active
RWMC-PRO-A-064	258	Production	Vadose Zone	Inactive
M4D	255	Observation	Aquifer	Active
WHEATGRASS DEPT. WATER	251	Production	Aquifer	Active
USGS-133	249	Corehole	Aquifer	Active
LF2-10	249	Observation	Aquifer	Active
USGS-008	247	Observation	Aquifer	Active

7.4 Well Integrity Logs and/or Testing

Well integrity logs are not applicable for any of the wells at the proposed FORGE site.

7.5 Ease of Drilling

The most difficult drilling encountered in INEL-1 was in the upper 450 m (1,476 ft) of the borehole—in the upper fractured basalts and sediments. The rate of penetration for this interval was 29 m (95 ft) per day. This zone is subject to lost circulation due to the extremely large voids and high permeability of the basalts. The upper portion of the hole is also the largest diameter and the first part of the project where it is common to suffer from startup difficulties. Below 450 m (1,476 ft), the rate of penetration for INEL-1 was approximately 67 m (220 ft) per day. The rate-of-penetration chart is presented in Figure 30.

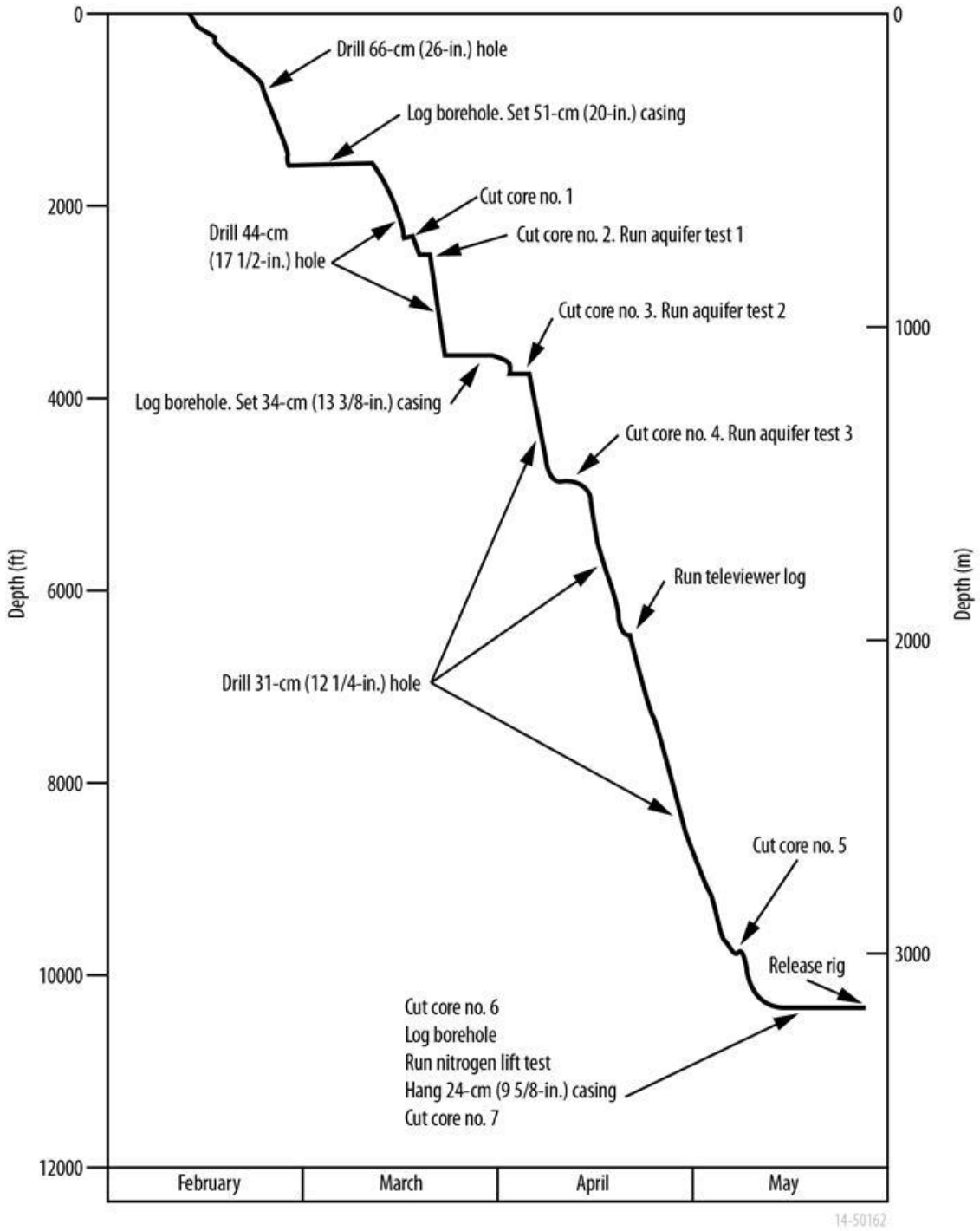

Figure 30. Rate of drilling penetration and operations summary form for INEL-1 (Prestwich and Bowman, 1980).

REFERENCES

Ackerman, D.J., et al., 2006, A Conceptual Model of Ground-Water Flow in the Eastern Snake River Plain Aquifer at the Idaho National Laboratory and Vicinity with Implications for Contaminant Transport: United States Geological Survey SIR 2006-5122, U.S. Department of the Interior, 62 p.

Arnórsson, S., Gunnlaugsson, E., and Svavarsson, H., 1983, The chemistry of geothermal waters in Iceland. III. Chemical geothermometry in geothermal investigations: Geochimica et Cosmochimica Acta, vol. 47, no. 3, p. 567–577.

Bakshi, R., Halvaei, M., and Ghassemi, A., 2016, Geomechanical characterization of core from the proposed FORGE laboratory on the eastern Snake River Plain, Idaho, *in* Proceedings, 41st Workshop on Geothermal Reservoir Engineering, SGP TR 209: Stanford University, Stanford, California.

Bates, D.L., 1999, The in situ chemical fractionation of an eastern Snake River Plain basalt flow: implications for heterogeneous chemical interaction with groundwater contaminants, in Geology: Idaho State University, Pocatello, Idaho, 146 p.

Blackwell, D., 1989, Regional implications of heat flow of the Snake River Plain, northwestern United States: Tectonophysics, v. 164, no. 2, p. 323–343.

Blackwell, D., Kelly, S., and Steele, J., 1992, Heat flow modeling of the Snake River Plain, Idaho: Idaho National Laboratory, Idaho Falls, Idaho, 109 p.

Blackwell, D., and Richards, M., 2004, Calibration of the AAPG geothermal survey of North America BHT database, *in* AAPG Annual Meeting: Dallas, Texas.

Blackwell, D., Steele, J.L., and Carter, L.S., 1991, Heat flow patterns of the North American continent: A discussion of the DNAG geothermal map of North America, *in* Engdahl, E.R., and Blackwell, D.D., e.D.B.S, in Neotectonics of North America, Geological Society of America, DNAG, p. Map, 1:423437.

Brott, C.A., Blackwell, D., and Mitchell, J.C., 1976, Geothermal investigations in Idaho, Part 8, heat flow studies of the Snake River Plain, Idaho: Idaho Department of Water Resources Water Information Geological Society of America Bulletin, v. 30, 159 p.

Bruhn, R.L., Wu, D. and Lee, J.J., 1992, Final Report on the Structure of the Southern Lemhi and Arco Fault Zone, Idaho: Idaho Falls, Idaho: EG&G Informal Report, Idaho National Laboratory, 26 p.

Carpenter, N.S., Payne, S.J., Hodges, J.M., and Berg, R.G., 2011, INL Seismic Monitoring Annual Report: January 1, 2010 – December 31, 2010: Idaho National Laboratory Report INL/EXT-11-23143, 13 p.

Doherty, D.J., L.A. McBroome, and M.A. Kuntz, 1979, Preliminary geological interpretation and lithologic log of the exploratory geothermal test well (INEL-1), Idaho National Engineering Laboratory, eastern Snake River Plain, Idaho: United State Geological Survey Open-File Report 79-1248, 9 p.

Doser, D.I., and Smith, R.B., 1985, Source parameters of the 28 October 1983 Borah Peak, Idaho, earthquake from body wave analysis: Bulletin of the Seismological Society of America, v. 75, no. 4, p. 1041–1051.

Du, Y., and Aydin, A., 1992, Three dimensional characteristics of dike intrusion along the northern Iceland rift from inversion of geodetic data: Tectonophysics, v. 204, p. 111–121.

Eddington, P.K., Smith, R.B., and Renggli, C., 1987, Kinematics of Basin and Range intraplate extension: Geological Society, London, Special Publications, v. 28, no. 1, p. 371–392.

Fournier, R.O., and Potter, R.W., II, 1979, Magnesium correction to the Na-K-Ca chemical geothermometers: Geochimica et Cosmochimica Acta, vol. 43, p 1543–1550.

Fournier, R.O., and Truesdell, A.H., 1973, An empirical Na-K-Ca geothermometer for natural waters: Geochimica et Cosmochimica Acta, vol. 37, p. 1255–1275.

Hackett, W.R., Smith, R.P., and Khericha, S., 2002, Volcanic hazards of the Idaho National Engineering and Environmental Laboratory, southeast Idaho, *in* Bonnichsen, B., White, C.M., and Curry, M., eds., Tectonic and Magmatic Evolution of the Snake River Plain Volcanic Province, Idaho: Idaho Geol. Surv. Bull., v. 30, no. 461–482, 461 p.

Hadley, D.M., and Cavit, D.S., 1984, Sierra Geophysics Report: Geophysical Investigations at the Idaho National Engineering Laboratory, EG&G Idaho Report No. SGI R 84 111, 73 p.

Hemphill-Haley, M.A., et al., 2000, Timing of faulting events from thermoluminescence dating of scarp-related deposits, Lemhi fault, southeastern Idaho: AGU Reference Shelf, v. 4, p. 541–548.

Hildenbrand, T., et al., 2000, Regional crustal structures and their relationship to the distribution of ore deposits in the western United States, based on magnetic and gravity data: Economic Geology, v. 95, p. 1583–1603.

Hughes, S.S., et al., 1999, Mafic volcanism and environmental geology of the eastern Snake River Plain, Idaho, *in* Guidebook to the Geology of Eastern Idaho: Pocatello, Idaho, Museum of Natural History, p. 143-168.

ISRM, 1978, Suggested Methods for Determining Tensile Strength of Rock Materials: International Journal of Rock Mechanics and Mining Sciences and Geomechanics, Abstracts, p. 99–100.

Jackson, S.M., et al., 1989, The 1988 INEL Microearthquake Survey near the Western Edge of the Eastern Snake River Plain: Idaho National Laboratory.

Jackson, S.M., et al., 2006, Seismic Reflection Project Near the Southern Terminations of the Lost River and Lemhi Faults, Eastern Snake River Plain, Idaho: Idaho National Laboratory, INL/EXT-06-11851, 16 p.

Johnson, T.M., et al., 2000, Groundwater Fast Paths' in the Snake River Plain Aquifer: Radiogenic Isotope Ratios as Natural Groundwater Tracers: Geology, no. 28, p. 871–874.

Kelbert, A., and Egbert, G., 2012, Crust and upper mantle electrical conductivity beneath the Yellowstone Hotspot Track: Geology, v. 40, no. 5, p. 447–450.

Knutson, C.F., McCormick, K.A., Smith, R.P., Hackett, W.R., O'Brian, J.P., and Crocker, J.C., 1990, FY 89 report Radioactive Waste Management Complex vadose zone basalt characterization: EG&G Idaho Report EGG-WM-8949, 412 p.

Kuntz, M.A., Covington, H., and Schorr, L., 1992, An overview of basaltic volcanism of the eastern Snake River Plain, Idaho, *in* Link, P.K., Kuntz, M.A., and Platt, L.B., eds., Regional geology of eastern Idaho and western Wyoming: Geological Society of America Memoirs, p. 227–267.

Kuntz, M.A., et al., 1994, Geologic map of the Idaho National Engineering Laboratory and adjoining areas, Eastern Idaho: U.S. Geological Survey M.I. Series, Map I-2330, scale 1:000,000.

Lanphere, M.A., Champion, D.E., and Kuntz, M.A., 1993, Petrography, age, and paleomagnetism of basalt lava flows in coreholes Well 80, NRF 89-04, NRF 89-05, and ICPP 123, Idaho National Engineering Laboratory; U.S. Geological Survey Open-File Report Report 93-327, 57 p.

Lanphere, M.A., Kuntz, M.A., and Champion, D.E., 1994, Petrography, age, and paleomagnetism of basaltic lava flows in coreholes at Test Area North (TAN): U.S. Geological Survey Open-File Report Report 94-686, 49 p.

Leeman, W.P., Schutt, D.L., and Hughes, S.S., 2009, Thermal structure beneath the Snake River Plain: Implications for the Yellowstone hotspot: Journal of Volcanology and Geothermal Research, v. 188, no. 1-3, p. 57–67.

Link, P.K., Fanning, C.M., and Beranek, L.P., 2005, Reliability and longitudinal change of detrital-zircon age spectra in the Snake River system, Idaho and Wyoming: an example of reproducing the bumpy barcode: Sedimentary Geology, v. 182, no. 1, p. 101–142.

Mabey, D.R., 1982, Geophysics and tectonics of the Snake River Plain, Idaho, *in* Bonnichsen, B., and Breckenridge, R.M., eds., Cenozoic Geology of Idaho, Idaho Geological Survey Bulletin, v. 26, p. 139-154.

Mankinen, E.A., et al., 2004, Guide to Geophysical Data for the Northern Rocky Mountains and Adjacent Areas, Idaho, Montana, Washington, Oregon, and Wyoming: U.S. Geological Survey Open-File Report Report 2004-1413, p. 34.

Mann, L.J., 1986, Hydraulic properties of rock units and chemical quality of water for INEL-1: a 10,365-foot deep test hole drilled at the Idaho National Engineering Laboratory, Idaho: U.S. Geological Survey Water Resources Investigations Report 86-4020.

McLing, T.L., et al., 2016, Temperature distribution aquifer geometry, and groundwater flow in the Snake River Plain aquifer, Eastern Snake River Plain, Idaho: Geological Society of America Bulletin (in press).

McLing, T.L., Smith, R.W., and Johnson, T.M., 2002, Chemical Characteristics of Thermal Water Beneath the Eastern Snake River Plain Aquifer: GSA Special Paper, no. 353, 13 p.

Meqbel, N.M., et al., 2014, Deep electrical resistivity structure of the northwestern US derived from 3-D inversion of USArray magnetotelluric data: Earth and Planetary Science Letters 402, p. 290–304.

Moos, D., and Barton, C., 1990, In-Situ Stress and Natural Fracturing at the INEL Site, Idaho, DOE Report EGG-NPR-10631.

Morgan, L.A., Doherty, D.J., and Leeman, W.P., 1984, Ignimbrites of the eastern Snake River Plain, Idaho: Evidence for major caldera-forming eruptions: Journal of Geophysical Research: Solid Earth (1978–2012), v. 89, p. 8665–8678.

Morse, L.H., 2002, Basalt alteration and authigenic mineralization near the effective Base of the Snake River Plain Aquifer at the Idaho National Engineering and Environmental Laboratory, Idaho, *in* Geology: Idaho State University, Pocatello, Idaho, 182 p.

Morse, L.H., and McCurry, M., 2002, Genesis of alteration of Quaternary basalts within a portion of the eastern Snake River Plain aquifer, *in* Link, P.K., and Mink, L.L., eds., Geological Society of America Special Paper 353: Geological Society of America, Boulder, Colorado, p. 213–224.

Neupane, G., et al., 2014, Deep geothermal reservoir temperatures in the Eastern Snake River Plain, Idaho using multicomponent geothermometry, *in* Proceedings, 39th Workshop on Geothermal Reservoir Engineering: Stanford, California, 12 p.

Nielson, D.L., Delahunty, C., and J.W. Shervais, 2012, Geothermal Systems in the Snake River Plain, Idaho, Characterized by the Hotspot Project: Geothermal Resources Council Transactions, v. 36, p. 727-730.

Nielson, D.L., and Shervais, J.W., 2014, Conceptual Model for Snake River Plain Geothermal Systems, *in* Thirty-Ninth Workshop on Geothermal Reservoir Engineering: Stanford, California, Stanford University.

NIRS, 2014, Rhyolite: http://www.nirs.go.jp/db/anzendb/NORMDB/ENG/norm_detail.php?norm=ore&en_normname=%CE%AE%CC%E6%B4%E4 - kekka.

Olig, S.S., 1997, Trench investigation of Butte City scarps, 4 plates, 12 p.

Olig, S.S., et al., 1997, Additional geological investigations of the southern Lost River fault and northern Arco rift zone, Idaho: unpublished report prepared by Woodward-Clyde Federal Services for Lockheed Martin Technologies Company, Project No. SK9654.

Pankratz, L.W. and Ackermann, H.D., 1982, Structure along the northwest edge of the Snake River Plain interpreted from seismic refraction: Journal of Geophysical Research: Solid Earth (1978–2012), v. 87, no. B4, p. 2676–2682.

Payne, S., et al., 2012, A new interpretation of deformation rates in the Snake River Plain and adjacent basin and range regions based on GPS measurements: Geophysical Journal International, v. 189, no. 1, p. 101–122.

Payne, S.J., Hodges, J. M., Berg, R.G., and Bruhn, D.F., 2011, INL Seismic Monitoring Annual Report: January 1, 2011 – December 31, 2011: Battelle Energy Alliance, 88 p.

Payne, S.J., McCaffrey, R., and King, R.W., 2008, Strain rates and contemporary deformation in the Snake River Plain and surrounding Basin and Range from GPS and seismicity: Geology, v. 36, no. 8, p. 647–650.

Payne, S.J., McCaffrey, R., King, R.W., and Kattenhorn, S.A., 2012, A new interpretation of deformation rates in the Snake River Plain and adjacent Basin and Range regions based on GPS measurements: Geophysical Journal, v. 189, p. 101–122.

Pierce, K.L., and Morgan, L.A., 1992, The track of the Yellowstone hot spot: Volcanism, faulting, and uplift: Geological Society of America Memoirs, v. 179, p. 1-54.

Pittman, J.R., 1994, Hydrological and meteorological data for an unsaturated zone study area near the Radioactive Wast Management Comples, Idaho National Engineering Laboratory, Idaho – 1988 and 1989: U.S. Geological Survey Open-File Report 95-112, p. 95–112.

Prestwich, S., and Bowman, J.A., 1980, Completion and testing report: INEL geothermal exploratory well one (INEL-1): U.S. Department of Energy, Idaho Operations Office, IDO-10096.

Richins, W.D., et al., 1987, The 1983 Borah Peak, Idaho, earthquake and its aftershocks: Bulletin of the Seismological Society of America, v. 77, no. 3, p. 694–723.

Roback, R.C., et al., 2001, Uranium isotopic evidence for groundwater chemical evolution and flow patterns in the eastern Snake River Plain aquifer, Idaho: Geological Society of America Bulletin, no. 113, p. 1133–1141.

Shervais, J.W., et al., 2011, Hotspot: The Snake River Geothermal Drilling Project—An Overview: Transactions-Geothermal Resources Council, v. 35, no. 2, p. 995–1003.

Shervais, J.W., et al., 2013, First Results from HOTSPOT: The Snake River Plain Scientific Drilling Project, Idaho, USA: Scientific Drilling, no.15, p. 36–45.

Smith, R.B., et al., 2009, Geodynamics of the Yellowstone hotspot and mantle plume: Seismic and GPS imaging, kinematics, and mantle flow: Journal of Volcanology and Geothermal Research, v. 188, no. 1, p. 26–56.

Smith, R.P., 2004, Geologic setting of the Snake River Plain aquifer and vadose zone: Vadose Zone Journal, v. 3, no. 1, p. 47-58.

Smith, R.P., Jackson, S.M., and Hackett, W.R., 1996, Paleoseismology and seismic hazards evaluations in extensional volcanic terrains: Journal of Geophysical Research: Solid Earth (1978–2012), v. 101, no. B3, p. 6277–6292.

Sparlin, M.A., Braile, L., and Smith, R.B., 1982, Crustal structure of the eastern Snake River Plain determined from ray trace modeling of seismic refraction data: Journal of Geophysical Research: Solid Earth (1978–2012), v. 87, no. B4, p. 2619–2633.

Stanley, W.D., 1982, Magnetotelluric soundings on the Idaho National Engineering Laboratory facility, Idaho: Journal of Geophysical Research: Solid Earth (1978–2012), v. 87, no. B4, p. 2683–2691.

Stickney, M.C., and Bartholomew, M.J., 1987, Seismicity and late Quaternary faulting of the northern Basin and Range province, Montana and Idaho: Bulletin of the Seismological Society of America, v. 77, no. 5, p. 1602–1625.

Waite, G.P., and Smith, R.B., 2004, Seismotectonics and stress field of the Yellowstone volcanic plateau from earthquake first motions and other indicators: Journal Geophysicist Resource, v. 109, B02301, doi:10.1029/2003JB002675.

Wannamaker, P.E., et al., 2008, Lithospheric dismemberment and magmatic processes of the Great Basin–Colorado Plateau transition, Utah, implied from magnetotellurics: Geochemistry, Geophysics, Geosystems, v. 9, no. 5.

Whitehead, R.L., 1992, Geohydrologic framework of the Snake River Plain regional aquifer system, Idaho and eastern Oregon: U.S. Geological Survey Professional Paper 1408-B, 32 p.

Wood, T.R., et al., 2007, Development Report on the Idaho National Laboratory Sitewide Three-Dimensional Aquifer Model: Idaho National Laboratory, INL/EXT-07-13337.

Wood, W.W., and Low, W.H., 1986, Aqueous Geochemistry and Diagenesis in the Eastern Snake River Plain Aquifer System, Idaho: Geological Society of America Bulletin, no. 97, p. 1456–1466.

Woodward-Clyde, 1992, Paleoseismic investigations of the southern Lemhi Fault, Idaho: EG&G Informal Report EGG-GEO-10178, p. 1–32.

Woodward-Clyde, 1995, Paleoseismic investigation of the southern Lost River fault zone, Idaho: Lockheed Idaho Technologies Company: Technical Report INEL-95/0508, p. 82.

Woodward-Clyde Federal Services, G.C., and Pacific Engineering and Analysis, 1996, Site Specific Seismic Hazard Analyses for the Idaho National Engineering Laboratory: Lockheed Idaho Technologies Company.

Zoback, M.L., and Zoback, M.D., 1989, Tectonic stress field of the continental United States: Geological Society of America Memoirs, v. 172, p. 523–540.

Zohdy, A., and Bisdorf, R., 1980, Deep Schlumberger soundings for geothermal exploration at INEL, Snake River Plain, Idaho: Geophysics, v. 45, p. 583–584.